The C1 wedge connection in towers for wind turbine structures, tensile behaviour of a segment test

Cheng, Lu; Yang, Fei; Winkes, Jasper Stefan; Veljkovic, Milan

DOI
10.1016/j.engstruct.2023.115799

Publication date
2023

Document Version
Final published version

Published in
Engineering Structures

Engineering Structures 282 (2023) 115799

Contents lists available at ScienceDirect

Engineering Structures

journal homepage: www.elsevier.com/locate/engstruct

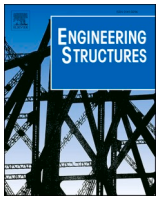

The C1 wedge connection in towers for wind turbine structures, tensile behaviour of a segment test

Lu Cheng [a,*], Fei Yang [b], Jasper Stefan Winkes [c], Milan Veljkovic [a]

[a] Faculty of Civil Engineering and Geosciences, Delft University of Technology, Delft, the Netherlands
[b] School of Civil Engineering, Chang'an University, Xi'an, China
[c] C1 Connections, The Hague, the Netherlands

ARTICLE INFO

Keywords:
C1 wedge connection
Experimental study
Bolted connection
Tensile behaviour
FE modelling

ABSTRACT

This paper shows a part of the analysis of the development of the second generation of the C1 wedge connections for use in offshore wind turbine supporting towers. The novelty of this connection is that bolt failure is avoided under static and fatigue loads. This study aims to investigate the tensile behaviour of the connection by combining the findings of experiments and finite element (FE) analysis. Two specimens subjected to uniaxial and cyclic tensile loading tested until failure are used for illustration. Advanced quasi-static FE analysis results, considering the most detailed geometry and using an explicit dynamic solver, are compared to the experimental results. The FE analysis results agree well with the experimental results. Based on the FE model, a parametric study is carried out to analyse the influence of the bolt grade, friction coefficient between contact surfaces, and preloading force level on mechanical behaviour. Failure modes, bolt force development, and the evolution of gap opening between contacted segments are analysed. Results demonstrate that the tensile fracture of the C1 wedge connection mainly appears in the lower segment. All the investigated parameters have a negligible effect on the connection's ultimate resistance and failure mode. However, the friction coefficient between contact surfaces and bolt preload level significantly affects the connection's local deformation capacity and the response of the bolt stress range. The FE simulation provides practical guidance for designing this connection without bolt failure.

1. Introduction

The potential of offshore wind power has attracted growing interest and record investment in offshore wind projects in recent years. €26 billion for the construction of new offshore wind farms in Europe was invested to finance 7.1GW of new offshore power capacity [1]. This reinforces the demand for the use of larger capacity and more efficient offshore wind turbines (OWTs). Meanwhile, the requirement for increasing the size of the supporting structures has been observed for the new generation of OWTs [2–4].

Supporting structures of OWT are commonly constructed of tubular towers and substructures [5,6]. The tubular towers are divided into a couple of shorter segments to facilitate transport. The connections between adjacent segments are key mechanisms to guarantee the integrity and stability of OWT structures. Various types of connections have been proposed by designers [3]. The bolted ring-flange connection (RF) is considered the most promising and common solution for OWT [7–13]. The design of the wind turbine towers is primarily dominated by the fatigue design of the bolted ring flange connection [14–17]. Design standards and recommendations provide bolt detail category 50 (if the bending stresses are included) [17,18]. A reduction factor should be considered for the fatigue resistance of bolts with a diameter larger than 30 mm [19,20]. A new generation of OWTs requires RF connections with much thicker ring flanges and larger bolts/studs with a diameter up to 80 mm (M80). However, a more comprehensive investigation is required due to these two reasons [3,21,22]: (1) current design processes, manufacturing tolerances, and construction is insufficient to apply larger ring flanges and bolts/studs optimally; (2) The fatigue performance of the RF connection with larger bolts (studs)/flanges needs to be quantitatively evaluated with an improved analytical model.

Recently finished research projects, OFWEC1 and OFWEC2 (Offshore Wedge Connection), introduced a novel connection called "C1 wedge connection" [23] as an alternative option for the new generation of OWTs. Compared to the conventional RF connections, the C1 wedge connection reduces the construction, installation and maintenance costs by eliminating the thick ring flange and using smaller diameter bolts

* Corresponding author.
E-mail address: L.cheng-2@tudelft.nl (L. Cheng).

https://doi.org/10.1016/j.engstruct.2023.115799
Received 17 June 2022; Received in revised form 27 January 2023; Accepted 10 February 2023
Available online 23 February 2023

[24].

As illustrated in Fig. 1, three generations of the C1 wedge connection have been developed so far to improve fatigue resistance. A detailed analysis of the first generation of the C1 wedge connection was conducted experimentally and numerically under monotonic and fatigue conditions [25,26]. The fracture occurred at the hole of the lower segment. Detail category 92 was obtained for the innovative C1 wedge connection, which demonstrates a noticeable improvement in the fatigue resistance compared to the detail category 50 of bolts in the ring flange connections [17,18]. The C1 wedge connection is locally weakened by the presence of the holes (Fig. 1). To guarantee the resistance of the cylindrical tower (monopile), a set of analytical calculations is carried out e.g. the net section resistance in the smallest cross sections. A full-scale finite element (FE) model was built to investigate the global structural behaviour of the tower using C1 wedge connections [26]. The considered tower segments were 15 m long on both sides of the connection with an outer diameter of 7 m. The design procedure and related analytical model were proposed and validated. After that, the forged upper segment in the first-generation design is modified to a pinned-assembly in the upper segment, see Fig. 1 (b). As seen in Fig. 1 (c), additional improvements in the third generation of C1 wedge connections are related to the integration of the upper segment with webs by using butt welds.

Full-scale tests were performed on a 4.5 m-diameter tower within the OFWEC3 project (Fig. 2) and in-situ tower installation within the Arcadis Ost project (Fig. 3). As shown in Fig. 2, the personal-free tower alignment was successfully performed. Bolts were then fastened from the inside of the tower during the execution of the C1 wedge connection. Both ultimate limit state (ULS) and fatigue limit state (FLS) resistance was tested in the full-scale tests. These tests demonstrated quick and easy execution of the C1 wedge connection. The C1 wedge connection has been successfully certified by DNV in 2021 [27], and it is anticipated to be continually developed to minimise the costs of the welding but keep the main concept unchanged.

This paper aims to provide the investigation of the mechanical and functional performance of the second generation of the C1 wedge connection. The ultimate resistance and failure mechanism of the downscale segment using this type of C1 wedge connection under axial tensile load and low cycle load are described. In addition, detailed finite element (FE) models are established and non-linear analysis is carried out using ABAQUS with the damage model. The verified FE model helps to explain the load transfer mechanism of the second generation of the C1 wedge connection. Finally, parametric analysis is performed to build confidence in using the C1 wedge connection in engineering practice.

2. Experimental program

2.1. Geometry of the C1 wedge connection

Fig. 4 shows the schematic layout of the investigated connection. In the second generation of the C1 wedge connection, the upper segment and the lower segment are assembled to the webs by two kinds of connections: pinned connections and wedge connections. Elongated holes are machined in the lower segment and webs. The specific wedge connection comprises the horizontal bolt, wedges and blocks with an inclined plane. The slope of the wedge is consistent with the blocks. The imposed tensile load is transferred through the pined connection to the webs, followed by the movement of the fastener assembly connection and then to the lower segment.

In terms of the assembly procedure, a fork-shaped upper segment is obtained by pre-installing the pinned connection at first, see Fig. 5 (a). Then, the fastener assembly of the wedge connection is placed in the holes (Fig. 5 (b)). Due to the specific design of the holes, the fastener is only in contact with the top of the hole in the lower segment and the bottom of the holes in the webs, as shown in the origin line in Fig. 4. The pretension of the horizontal bolt causes the movement of two blocks corresponding to the increment of forces F_1, F_2 and F_3 ($F_1 + F_2 = F_3$), which in turn generates the contact pressure F_{pressure} (F_4) between the segments (Fig. 5 (c) and (d)). As presented in Fig. 5 (c), the relationship between the bolt pretension force P_c and the generated contact pressure F_{pressure} is:

$$F_{\text{pressure}} = F_4 = P_c / (tan(\alpha) + \mu) \quad (1)$$

2.2. Description of the specimen

Two specimens of the tower segment under tensile force were tested to understand the response of this type of C1 wedge connection (WC) in the segment specimen. The tests were performed in the Structures Laboratory at the Faculty of Civil Engineering and Geosciences, TU Delft. The specimens were scaled down to 1:4 of the prototype with the exact geometric dimensions. The main parameters of these specimens are shown in Fig. 4 and Table 1. The specimens were denoted as WC1 and WC2. As expressed in Eq. (1), the lower friction coefficient μ between the zinc-nickel coated wedge and block inclined plane generates the higher contact pressure. To perform a comparative study, different lubrication states about this contact pair are set for WC1 and WC2, respectively (see Table 1). The plate components were made of S460 steel grade for all specimens while the machined parts were made of 34CrNiMo6 steel with a minimum yield strength of 600 MPa. Grade 8.8

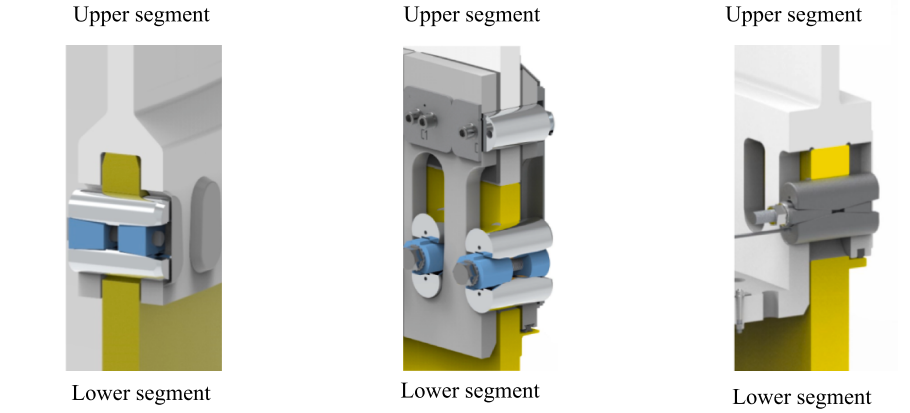

(a) First generation with forged upper segment

(b) Second generation with pinned-assembly upper segment

(c) Third generation with welded upper segment

Fig. 1. Development of C1 Wedge connection.

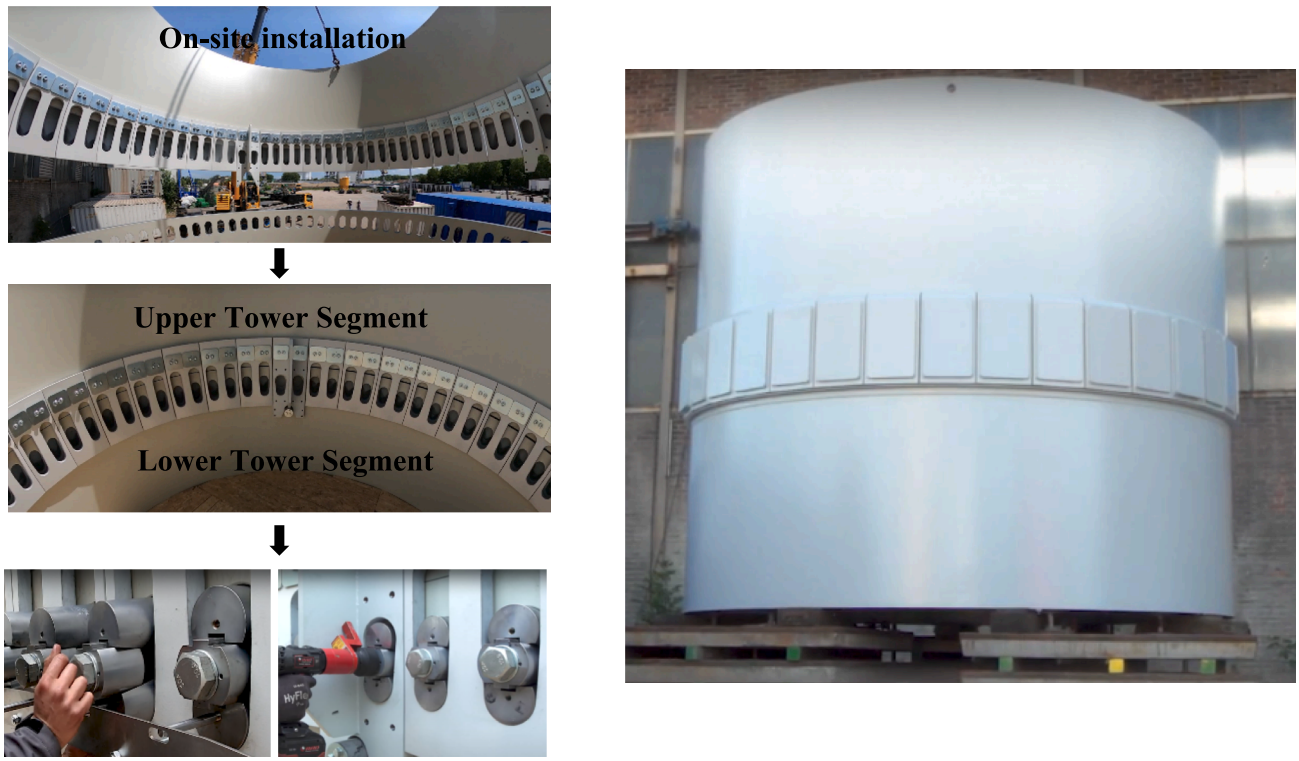

Fig. 2. Performed full-scale tests in OFWEC3 project [23].

Fig. 3. In-situ installation of the tower with C1 wedge connection [23].

high-strength M18 bolts were used in the connection. All bolt threads are lubricated as it is helpful to prevent bolt loosening and thread damage [28]. The lubrication mentioned in this paper is applied with MoS_2 grease.

2.3. Experimental set-up and instrumentation

A dedicated test setup was developed to perform the static tension test (see Fig. 6) because the capacity of the fatigue test set-up (see in [24]) is insufficient to test this connection to static tensile failure. The lower segment of the wedge connection was welded to a bottom plate. The upper segment was welded to an adaptor which is connected to a top plate with an M56 threaded bolt. The top and bottom plates were bolted to two rigid columns with eight bolts to ensure the rigidity of the entire loading system. Quasi-static loadings were applied through a hollow plunger cylinder with a capacity of 1000 kN.

The applied load N_Z, bolt forces and displacements in Z direction in the connection were measured during the experiments (Fig. 6). A digital manometer was used to record the pressure in the cylinder connected to the applied load. D1-D3 are linear variable differential transformers (LVDTs). In detail, D1 measured the displacement of the cylinder to determine the axial deformation of the specimens. D2-D3 were used to measure the gap opening between the connecting segments. The bolt was instrumented with a load cell to calibrate and control the tensile force in the bolt. The total length of the load cell is 100 mm.

Loading procedures of both specimens were divided into two steps: (1) Applied preloading force to the bolts P_c, and (2) imposed tensile forces N_Z on the specimen. Two levels of bolt preloading force P_c have been applied on these two specimens, as listed in Table 1. To explore the mechanical behaviour of the connections under various load levels, two loading protocols with a multi-stage loading method were designed for two specimens, as shown in Fig. 7. The yield load of the connection N_y is calculated using the measured yield strength of S460 material ($f_y = 485$ MPa) and the net cross-section area of the lower segment ($A_s = d_1 \times (b_1\text{-}d_2) = 1296$ mm^2). During the tension loading stage, force and displacement control were used to monitor the load applied to the specimen before and after the ultimate strength of the specimens.

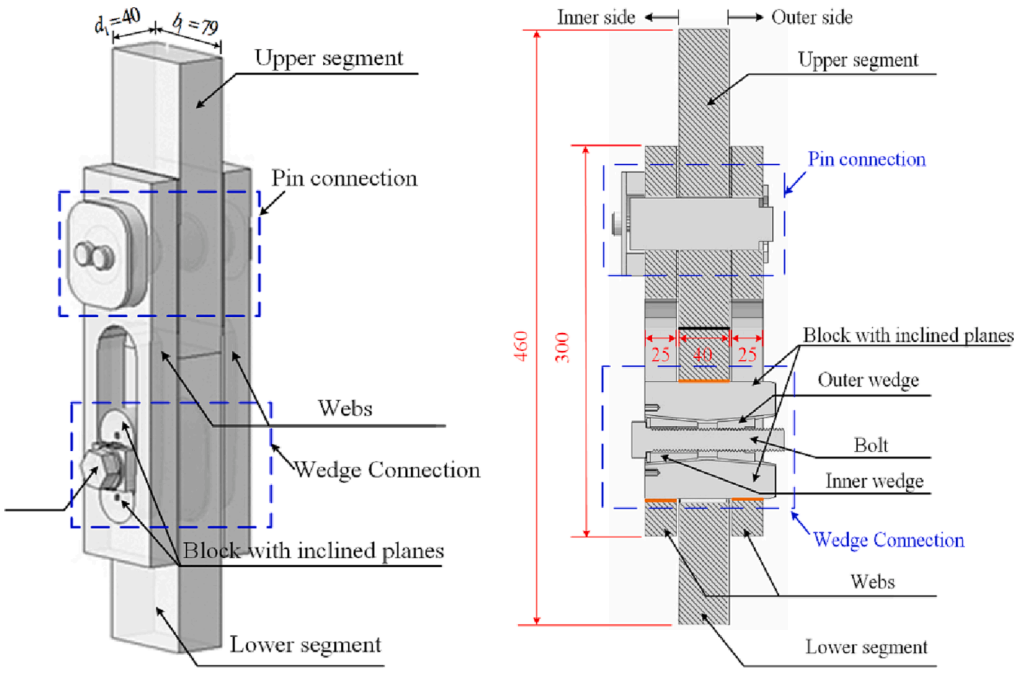

Fig. 4. Illustration of a segment specimen (unit: mm).

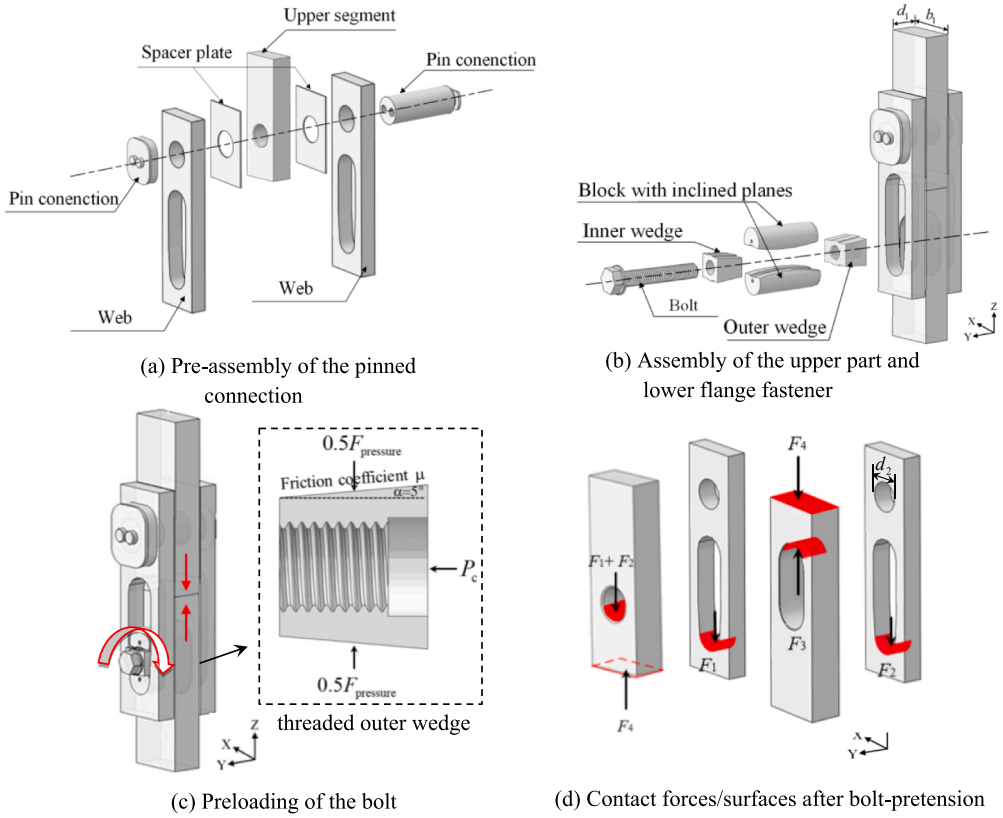

Fig. 5. Schematic views of tower segment with the C1 wedge connection in the study.

3. FE simulation

3.1. Basic modelling consideration

The finite element (FE) model of the C1 wedge connection is established using ABAQUS/Explicit for analysing its tensile behaviour. The geometry and boundary conditions of the segment models of the C1 wedge connection used in FE analysis are shown in Fig. 8 (a). The model comprises all tested specimen's components: rolled plate components and machined components. The connectors are modelled with the actual geometry, and all components (i.e., bolt, washer, inner wedge, outer wedge, blocks) are illustrated as separate parts. The threaded bolt and

Table 1
Main parameters of the specimens.

Specimen	P_c (kN)	Lubricated		Experimental results (kN)			FE analysis results (kN)			Comparison		
		Bolt threads	Wedge/block inclined plane	$N_{c,E}$	$N_{y,E}$	$N_{u,E}$	$N_{c,F}$	$N_{y,F}$	$N_{u,F}$	$N_{c,F}/N_{c,E}$	$N_{y,F}/N_{y,E}$	$N_{u,F}/N_{u,E}$
WC1	95	Yes	No	376	607	861	387	626	813	1.03	1.03	0.94
WC2	80	Yes	Yes	436	625	873	465	629	814	1.07	1.01	0.93

Note: The first subscript c means critical load at the end of the elastic stage, y and u mean the overall yield and ultimate resistance of the specimens. The second subscript E and F stand for results from experiments and FE analysis, respectively.

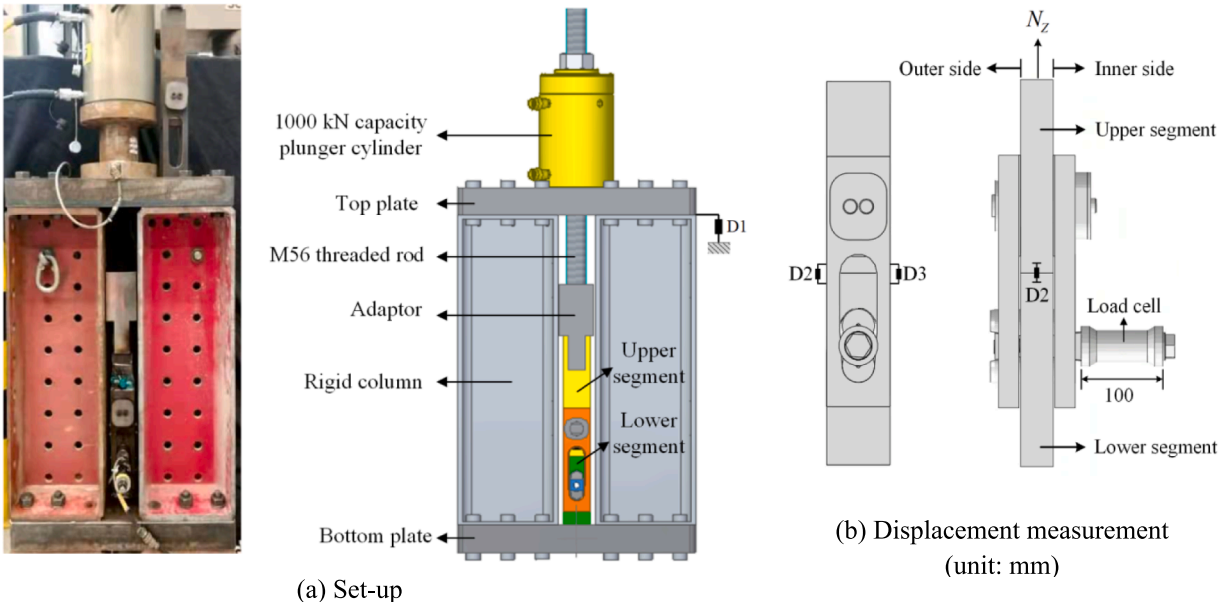

Fig. 6. Experimental system.

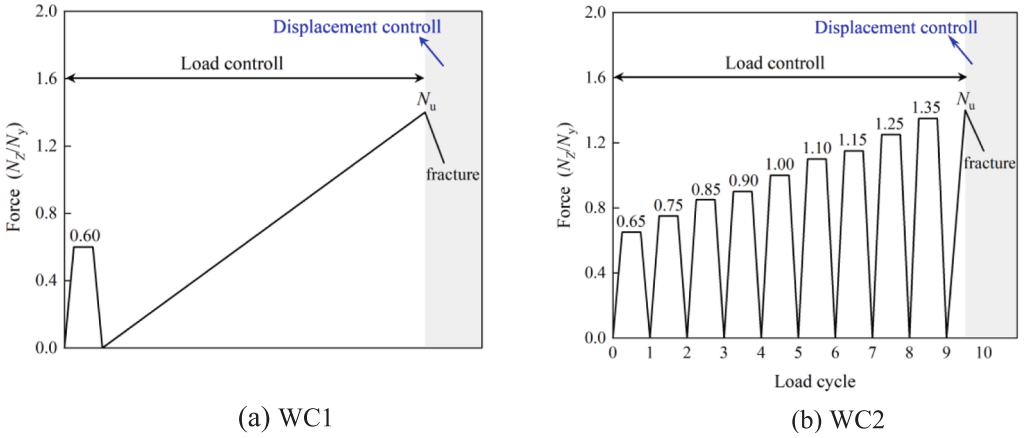

Fig. 7. Loading protocols for specimens WC1 and WC2.

outer wedge are modelled with actual dimensions, see Fig. 8 (b), to model as realistic as possible the complex interactions of the connector's components. It should be noted that, due to the complexity of the wedge connection and the high computer consumption of the explicit calculation, the upper segment welded to the test set-up is excluded in the model.

As presented in Fig. 8, appropriate boundary conditions are set for the reference points. The upper and lower cross-section surfaces are kinetically coupled to the reference points at the middle of the related surface RP1 and RP2, respectively. Fixed support boundary conditions are applied to RP2. Since a part of the deformation of the test set-up is included in the measured displacement, an elastic spring connected to the RP1 is added to account for the elastic deformation of the test set-up and the non-modelled welded part. The equivalent deformation of the entire specimen Δ can be obtained by Eqs. (2) and (3):

$$\Delta = N_Z/K_t = N_Z/K_s + N_Z/K_{WC} \tag{2}$$

$$K_s = K_t K_{WC}/K_{WC} - K_t \tag{3}$$

where N_Z is the tensile force; K_t, K_{WC}, and K_s represent the stiffness of the

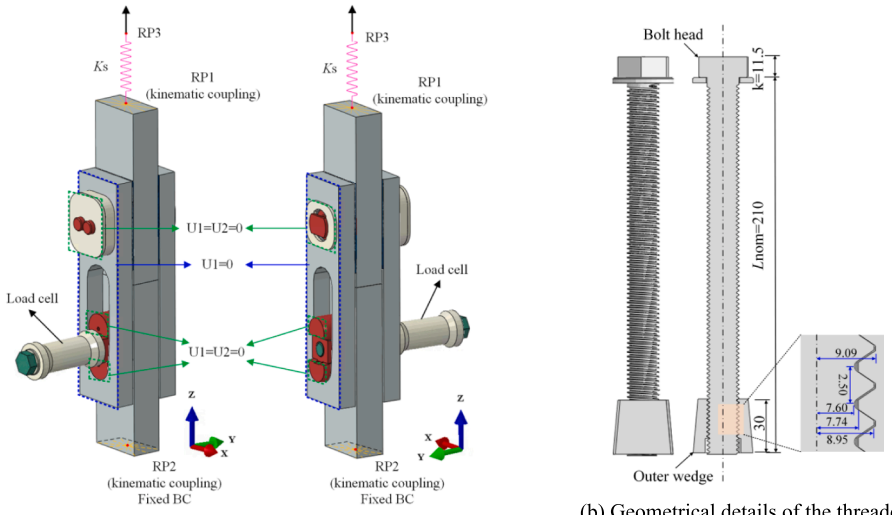

(a) Geometry and boundary conditions

(b) Geometrical details of the threaded bolt and outer wedge (unit: mm)

Fig. 8. Illustration of FE models.

experimental set-up, specimen, and spring, respectively. K_t is calculated as 219 kN/mm based on the test results. After several trials, K_s is estimated as 275 kN/mm for the analysis and contributes to around 80% of Δ.

3.2. Elements types and contact properties

Solid elements are used to model all components of the C1 wedge connections. Mesh details of the FE model are illustrated in Fig. 9. The plate components are meshed using eight-node hexahedron linear solid elements with reduced integration (C3D8R). The machined components, namely the bolt, threaded outer wedge, blocks and pin-bar with more complex geometry, are meshed with ten-node modified quadratic tetrahedron elements (C3D10M) to realise the free mesh. A global element size of 3 mm is applied to the bolts, inner wedge and outer wedge, while 1 mm is for the thread areas. A gradient grid with a maximum size of 10 mm is employed for the upper segment, lower segment and two webs. In the area of plate components close to the fastener assembly, the mesh size is refined to 2 mm.

According to VDI 2230 standard for bolted joints, the friction coefficient value of 0.04–0.1 is suggested for MoS_2-lubricated surfaces and 0.14–0.24 for zinc-nickel coated surfaces, respectively [29]. To reduce the computational cost and avoid convergence problems, general contact with a "penalty" tangential behaviour and a "hard" normal behaviour is selected to simulate all contact interactions in the specimen. As discussed before, the contact pressure between segments is sensitive to the friction coefficient μ of the inclined planes in the assembly of the wedge connection. Hence, the friction coefficient defined in the general contact is determined by the lubricant states between the wedge and block inclined plane. The friction coefficient μ of 0.18 is assumed for WC1 without wedge-block lubrication, while a conservative friction coefficient value of 0.1 is set for pre-lubricated WC2. The selection of these two values can also be calibrated based on the critical load N_c from test results. This is because the imposed load N_Z reaches N_c when the contact pressure $F_{pressure}$ (i.e. F_4) degrades to zero. Hence, the contact force F_4 is roughly identical to the N_c measured from the test. The friction coefficient μ can then be derived with the known preload force P_c and the contact force F_4.

3.3. Material models

The mechanical properties of the materials used in the FE model are listed in Table 2. Five materials are defined for the current study. (1) S460 structural steel for the plate components, shown in grey in Fig. 8; (2) Grade 8.8 /10.9 high strength steel for the M18 bolt, shown in green in Fig. 8; (3) 34CrNiMo6 steel for the machined components in the

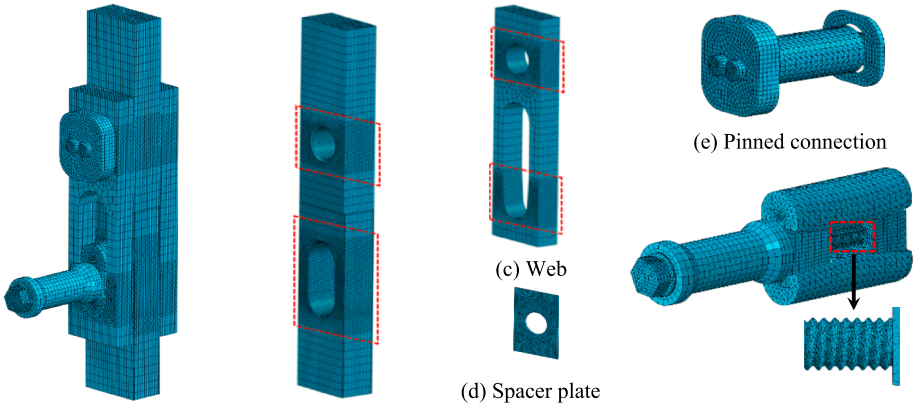

(a) Overview of the model

(b) Upper and lower segment

(c) Web

(d) Spacer plate

(e) Pinned connection

(f) Wedge connection

Fig. 9. Details of the FE mesh of all components.

Table 2
Material properties.

Component	Density	Young modulus	Steel grade	Yield strength	Ultimate strength	Peak strain	Ultimate elongation
	ρ (kg/m^3)	E_0 (MPa)		f_y (MPa)	f_u (MPa)	ε_u	A (%)
Plate	7850	2.1×10^5	S460	485	620	0.125	23
Fastener assembly	7850	2.1×10^5	34CrNiMo6	620	800	–	15
Nylon layer	1350	2.76×10^5	–	–	–	–	–
Load cell/pin connection	7850	2.1×10^5	–	–	–	–	–
M18 bolt	7850	2.1×10^5	8.8	776	970	0.05	10
			10.9	945	1050	0.05	10

fastener assembly, shown in red in Fig. 8; (4) Nylon material for the inserted nylon layer as spacer plate; (5) Elastic material for the load cell and pin connection, shown in white in Fig. 8. Poisson ratio $\nu = 0.3$ is used for all the components in the FE model. The conventional bilinear isotropic hardening model is not applicable to post-peak behaviour. Hence, the full-range stress–strain constitutive model is used for S460 steel and the bolt, which is explained in section 3.2.1. The damage is expected to occur in the low segment with the smallest cross-section area. Therefore, only the fracture mechanisms of S460 steel are considered in this study.

3.3.1. *Full-range true stress–strain constitutive material model*

It is assumed that the specimen volume remains constant in a uniaxial stress state up to the necking point. The prior-necking true stress–strain relations can be converted from the engineering stress–-strain curve, as expressed in Eqs. (4) and (5).

$$\sigma_t = \sigma_e(1+\varepsilon_e) \tag{4}$$

$$\varepsilon_t = ln(1+\varepsilon_e) \tag{5}$$

where σ_e and ε_e mean the engineering stress and strain, measured from the coupon tensile test. σ_t and ε_t denote the true stress and strain, respectively.

The post-necking material behaviour could not be obtained simply through extensometer measurements on the coupon specimen due to the variation in the cross-sectional area and the plastic instability [30]. Ling [31] proposed a combined linear and power stress–strain law to describe the post-necking stress–strain relations. This method assumes the empirical low and upper bounds for the post-necking material behaviour with $0 \le W \le 1$, as expressed as:

$$\sigma_t = (W)(a\varepsilon_t + b) + (1-W)\left(K\varepsilon_t^n\right) \tag{6}$$

where $a = \sigma_{t,u}$, $n = \varepsilon_{t,u}$, $b = a(1\text{-}n)$; $K = a/n^n$. $\sigma_{t,u}$ and $\varepsilon_{t,u}$ represent the true stress and true strain at the onset of necking, which can be calculated according to Eqs. (4) and (5). Yang et al. [32,33] proposed that the weighting factor W could be calibrated with values even less than zero or larger than 1. In this paper, W is calibrated for the investigated steel in the range of −0.5 to 1.5. Fig. 10 shows the employed full-range stress–strain relationship for S460 steel in this study.

3.3.2. *Rice-Tracy fracture criterion*

To simulate the fracture of the material under tensile loading, the Void Growth Model [34,35] (VGM) based on the Rice-Tracey (RT) function is employed in this paper:

$$\bar{\varepsilon}_D^{pl} = \alpha \cdot exp(-\beta \cdot \eta) \tag{7}$$

The model has been coded into the ABAQUS as "ductile damage" [36], dependent on the stress triaxiality η. It is assumed that the ductility decreases exponentially with the increased stress triaxiality. Then, the material fracture is predicted to occur when the critical void growth index ($VGI_{critical}$) is reached. α and β are two material-dependent parameters, where β is generally taken as 1.5 and α is similar to $VGI_{critical}$ which can be calibrated from the test results [37]. The damage initiation

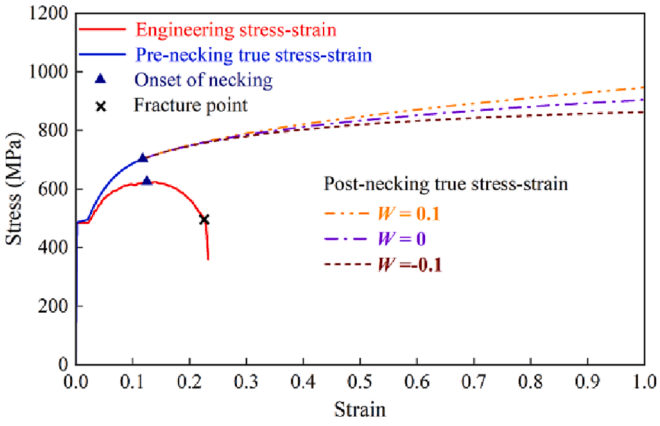

Fig. 10. Full-range stress–strain relationship of S460 steel.

criterion is reached when Eq. (8) is satisfied, in which $\bar{\varepsilon}^{pl}$ is the equivalent plastic strain (PEEQ) and the damage index W_D is the damage initiation variable.

$$W_D = \int d\bar{\varepsilon}^{pl} \Big/ \bar{\varepsilon}_D^{pl} = 1 \tag{8}$$

The mentioned RT criterion is taken as the damage initiation criterion. Damage evolution law is defined by the displacement type with a very small displacement, such as 0.001, at the failure to simulate a sudden load capacity loss after the damage initiation. Element deletion is triggered when $W_D = 1$ in the FE model.

3.3.3. *Material model calibration*

Tensile coupon tests were performed on S460 steel to formulate a full-range true stress–strain constitutive material model. Quasi-static analyses are performed using the explicit dynamic solver in ABAQUS. The coupons were cut from the same batch of S460 steel material used for the C1 wedge connection. The most appropriate W can be calibrated by comparing the engineering stress–strain curves from the FE results and the experimental results.

The mesh sensitivity analysis is carried out with two mesh sizes of 0.5 mm and 2.0 mm in the gauge parts with a length of 60 mm. Fig. 11 (a) and (b) show the comparison between the numerical and experimental engineering stress–strain curves for S460 steel using three weighting factors with an interval of 0.1. A larger weighting factor in the combined linear and power stress–strain law causes higher engineering stress in the descending stage. Meanwhile, a noticeable effect of the mesh size can be found in Fig. 11 (c) when the engineering strain is much larger than the fracture strain. The 0.5 mm mesh results in a sudden drop of load strength at a smaller fracture strain than the comparable one of the 2.0 mm mesh. This indicates that the strain localisation effect of the S460 steel is not sensitive to the mesh size before the PEEQ of 0.4. In conclusion, the weighting factor $W = 0$ and mesh size 2.0 mm are selected to describe the post-necking behaviour of S460 steel. A good agreement is obtained between the engineering strain–stress curve of S460 material from experimental and FE results, see Fig. 11 (d).

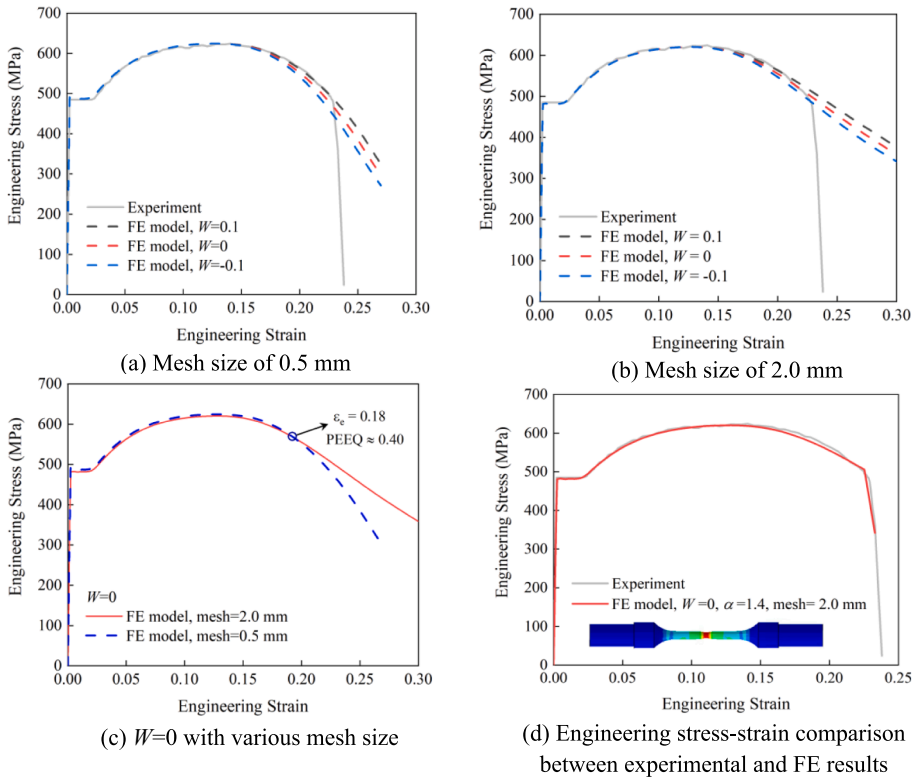

Fig. 11. Weighting factor calibration for S460 steel.

The yield strength of grade 8.8 and 10.9 bolts is determined using the nominal ratio f_y/f_u equals 0.8 and 0.9, respectively. Following Eqs. (4) and (5), the pre-necking true stress–strain curve can be obtained. Recent investigation indicates that the post-necking true stress–strain diagram for high-strength bolts under tensile loading can be described as a power strain–stress with a weight factor of 0 [32]. According to the experimental results on bolt material reported in [38,39], the full-range true stress vs. true strain curves for the bolt is obtained as shown in Fig. 12 (a).

For the sake of simplicity, idealised elastic–plastic-hardening properties are employed as the engineering stress–strain curve of 34CrNiMo6 steel, as shown in Fig. 12 (b). This is because no damage is expected in the machined parts of the wedge connection, where the maximum stress level in the FEA is about 400 MPa. Engineering stress–strain curves are converted into the true stress–strain curves for input in the ABAQUS plasticity model.

3.4. Loading procedure

Two calculation steps are carried out in the model to coincide with the physical test conditions. The bolt is preloaded first by the turn-of-bolt head method and then the model is loaded to the failure by applying the axial displacement to the tower segment. In the first step, as illustrated in Fig. 13, the edges of the bolt head are coupling constrained to the reference point RP-bolt located in the centre of the bolt head. A rotation is exerted on the RP-bolt around the centreline of the bolt. To reach the design preloading force P_c listed in Table 1, trial simulations are performed to determine the rotation angle. The preloading forces in

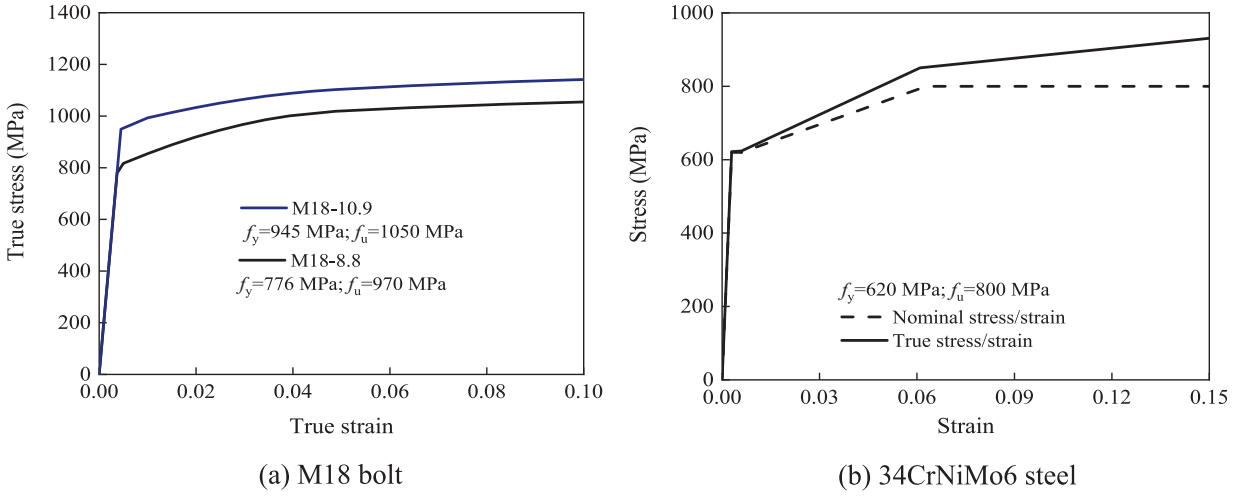

Fig. 12. Stress–strain curves for materials used in the bolt and machined components.

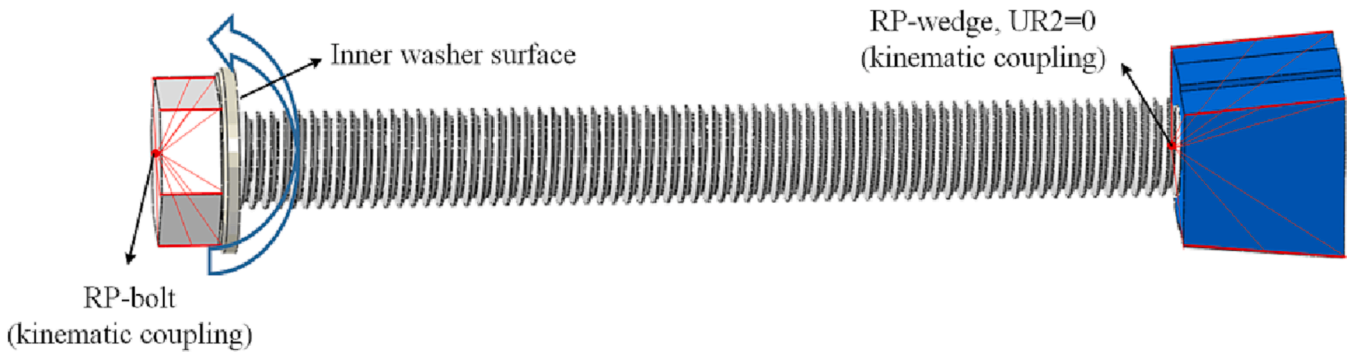

Fig. 13. Preloading of the bolts in the FE model.

the bolts are obtained by extracting the contact pressure force at the inner washer surface.

To perform quasi-static analysis, the explicit solver requires a conditional stability limit which can be approximated in terms of the material density ρ, the characteristic length of the smallest element L_e, and the Lamé parameters λ and μ:

$$\Delta t \approx min\left(L_c \cdot \sqrt{\rho/\lambda + 2\mu}\right) \tag{9}$$

The mesh verification analysis reveals that the smallest stable time increment in the FE model is 1.9×10^{-9}, leading to a large computational cost. These elements limiting the time increment are mainly from the bolt and outer wedge due to the threads, while the average stable time increment for other components is 2.0×10^{-7}. Considering the bolt and outer wedge are not critical components, a semi-automatic mass scaling option is used to shorten the computation time. As a generally accepted indication of the quasi-static analysis, the energy ratio between the kinetic energy to the internal energy should not be noticed throughout most of the simulation, not exceeding a small fraction (5%–10%). To achieve a trade-off between the computation time and accuracy of the FE model, the target time increment is set to be 1.0×10^{-6} s after several trial computations. The time periods adopted for preloading and loading to failure steps are 2.5 s and 0.25 s, respectively.

The contour plots along the meridional direction in the bolt and wedge connection for each specimen after preloading are shown in Fig. 14. Compared to the initial status, the inner and outer wedges approach at different distances due to the various bolt preload levels. Meanwhile, the bolt pretension causes the contact pressure F_4 between segments, as shown in Fig. 15. In the second step, an axial load is imposed by setting upward displacement of the reference point RP3 (Fig. 8).

4. Experimental and FE results

A corresponding comparison is made between the experimental and FE results shown below, separately for WC1 and WC2. The validated FE model is then used to conduct a parametric study to expand the experiments.

4.1. Behaviour of WC1

4.1.1. Failure mode

By observing the deformation of WC1 during the loading process with two cycles (Fig. 16 (a)), it can be found that the specimen maintains elasticity at the initial stage of the loading. The influence of the first loading-unloading cycle can be neglected within the elastic stage, representing a uniaxial tensile behaviour of the C1 wedge connection. The load–displacement curve in Fig. 16 (a) can be separated into three stages. The axial stiffness remains linear in the first stage. The imposed loading at the end of the elastic stage is defined as critical force $N_{c,E}$. After exceeding $N_{c,E}$, the axial stiffness decreases slightly with the increase of displacement. At the end of the second stage, the yield strength $N_{y,E}$ is achieved with a short yield plateau. After that, the specimen behaves nonlinearly, and the axial stiffness degrades gradually until the fracture of the specimen. The peak point of the curve is regarded as the overall axial ultimate resistance.

The relationships of applied load (Nz) versus the displacement from the experiments at the second cycle and FEA results of WC1 are presented in Fig. 16 (b). A good agreement between the experimental results and FE analysis results is achieved. The numerical values accompanied by the corresponding test results are presented in Table 1, with a maximum deviation of 7%. A small difference of 11 kN between $N_{c,F}$ and the $N_{c,E}$ verifies the selected friction coefficient μ of 0.18 for generating contact pressure.

Considering the tensile loading is dominantly transferred through the lower and upper segments, the distribution of PEEQ in the segments at four load levels is illustrated in Fig. 17. It can be found that local plastification occurs after exceeding the critical load of 387 kN. The lower segment experiences large plastic deformation successively with increasing the load.

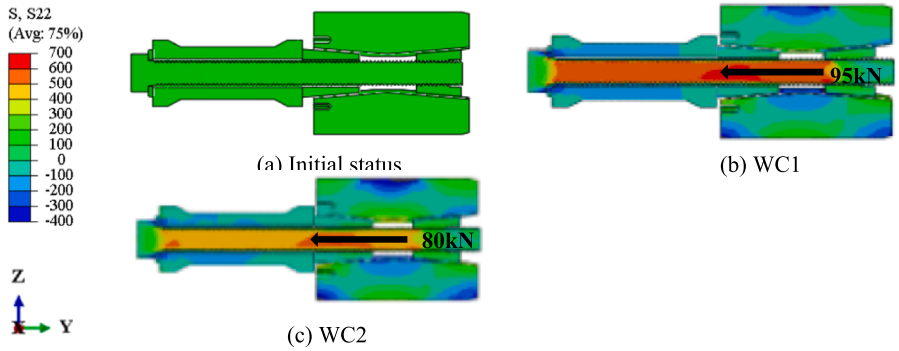

Fig. 14. Stress distribution and deformation of the fastener assembly of wedge connection.

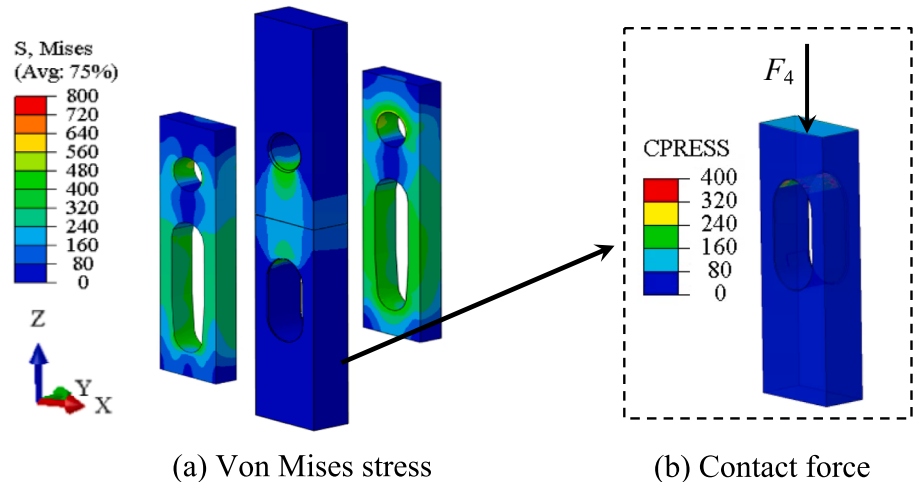

Fig. 15. Stress distribution of plate components after bolt preloading.

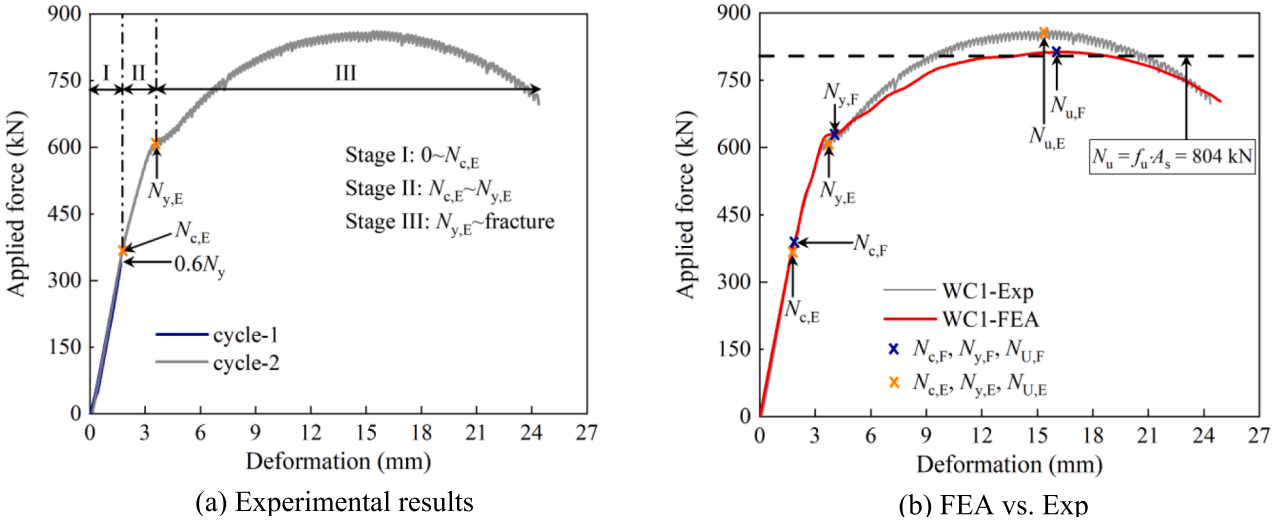

Fig. 16. Load–displacement curves of WC1.

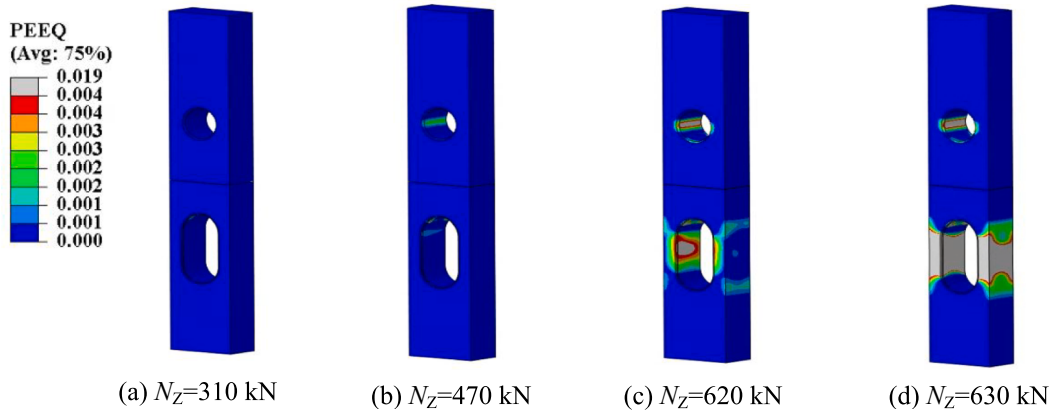

Fig. 17. PEEQ distribution in the lower and upper segment at four external loads N_z.

Fig. 18 shows the failure modes with residual deformation. Apparent necking failure of the lower segment is observed due to the smallest cross-section area A_s compared to the one in the upper segment. At the same time, the upper segment nearly remained undeformed. Hence, the bearing resistance of the specimen can be theoretically determined as $N_u = f_u \cdot A_s$ = 804 kN (see Fig. 16), where f_u is the ultimate strength of S460 steel. The comparison indicates that the failure mode depicted by the FE analysis reflects the failure process of the experimental specimens

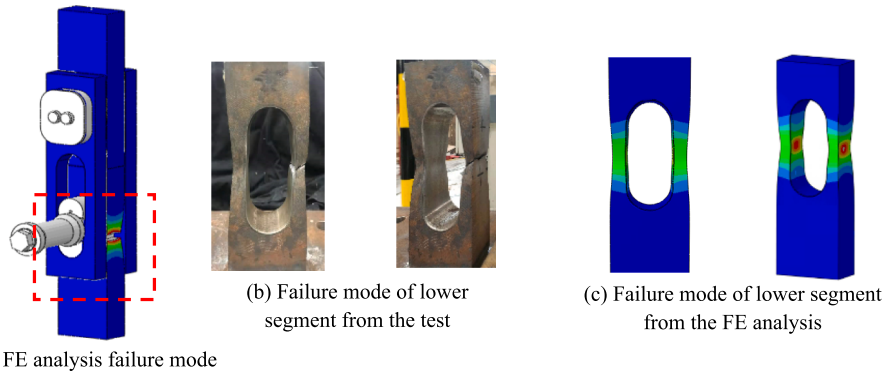

Fig. 18. Experimental and FE failure mode of WC1.

very accurately, as shown in Fig. 18.

4.1.2. Evolution of bolt force

Force in the bolt obtained from the load cell is shown in Fig. 19 (a). A slight decline during the first loading-unloading cycle is observed from the experimental results. The bolt force loss can be attributed to many reasons, among others the embedding loss as the contact interfaces in the connections which are usually not perfect with numerous protrusions. However, this fact can be neglected considering the elastic behaviour of the specimen at the initial stage of the loading. Similarly, the development of bolt force in WC1 includes three characteristic stages. Almost no change in the bolt force is observed in the first stage. In the second and third stages, the bolt force starts to increase nonlinearly with various gradient. Fig. 19 (b) shows the results of the bolt force versus the applied load curves from the experimental and FE simulation. An increasing scattering is observed between the test and FE results in the latest stage of loading.

The contact force responses are extracted from FE analysis in Fig. 20 to identify a point beyond which the increasing gradient of the bolt force appeared. The contact pressure F_4 between the upper and lower segment decreases linearly at first, while the contact forces F_1, F_2 and F_3 maintain the shape approximately with constant bolt force until the critical load $N_{c,F}$. Then, the low segment starts to support the imposed load, leading to an open connection and linearly increasing contact forces F_1, F_2 and F_3. It is obvious that the lower block in the C1-WC is subjected to bending as it spans two webs and the lower segment [24]. As F_1 and F_2 are increasing, the bolt receives the load transferred from the blocks with the increasing contact force at the wedge f_1 and f_2, (as shown in Fig. 21). The extraordinarily high contact pressure in Fig. 21 is attributed to a mathematical stress singularity that occurred in the steep corner. The stress singularity can be ignored considering these sharp corners are not critical areas for the mechanical behaviour of the specimen.

It is concluded that the bolt in the C1 wedge connection operates in two ways: (1) it introduces the contact pressure at the preloading stage; (2) it participates in the load transfer when reaching the critical load N_c. The calculation of WC1, shown in Fig. 19 is performed with a uniform friction coefficient of 0.18 for all contacts. However, the friction coefficient for lubricated bolt threads is much close to 0.1, which cannot be simulated via general contact used in the analysis. Consequently, the high friction coefficient leads to a larger bolt force than obtained in the test results beyond the critical load N_c, as shown in Fig. 19 (b). The results from the parametric analysis in section 5.1 demonstrate the maximum bolt force variation with a friction coefficient of 0.18 is 11 kN larger than with a smaller friction coefficient of 0.1, see Fig. 33. Similar influence of friction coefficient on bolted joints was also obtained in [40–43].

In terms of the tensile ultimate limit states (ULS), the final failure occurs in the lower segment instead of the bolt. It is observed that the maximum tensile stress of the bolt is below the yield strength. For fatigue limit states (FLS) resistance, the yield strength N_y is considered as the maximum applied fatigue load. The deviation of bolt force between

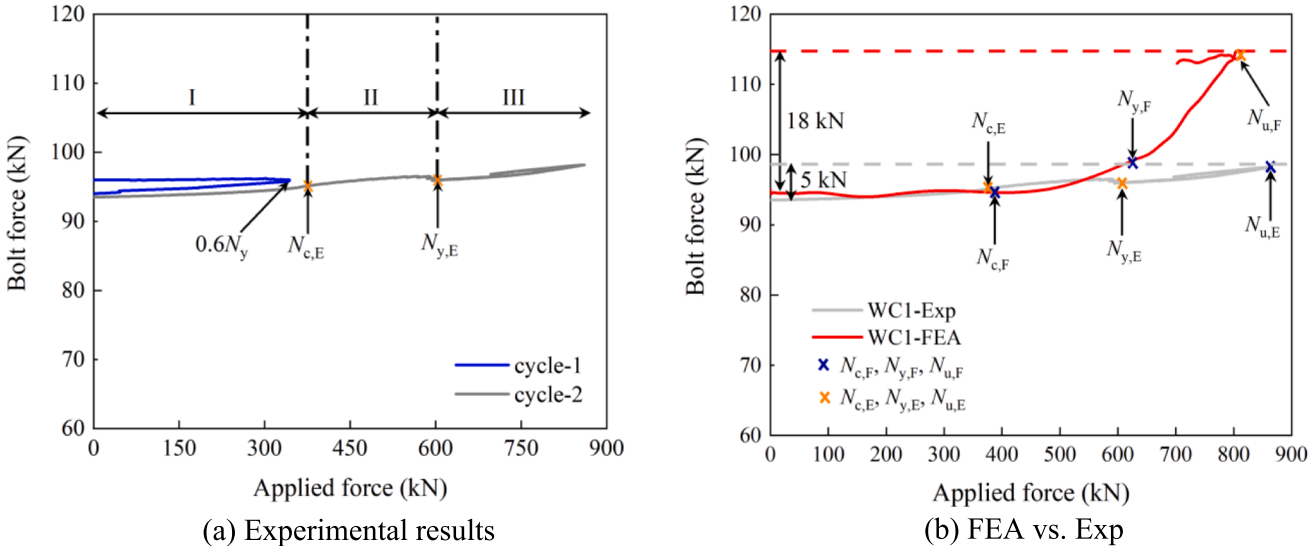

(a) Experimental results (b) FEA vs. Exp

Fig. 19. Evolution of bolt force of WC1.

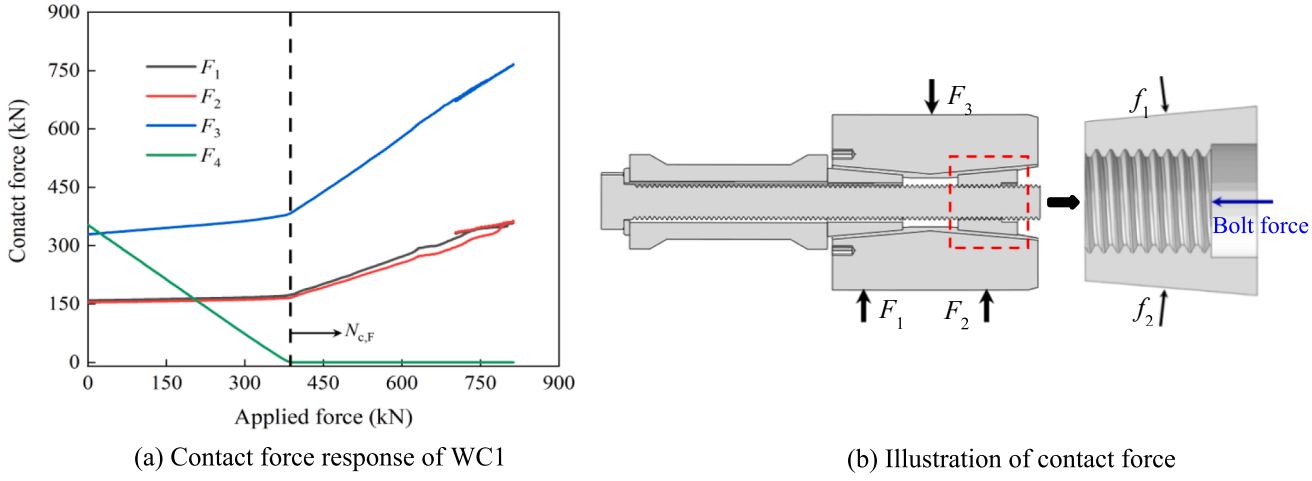

Fig. 20. Development of contact force of WC1 from FE analysis.

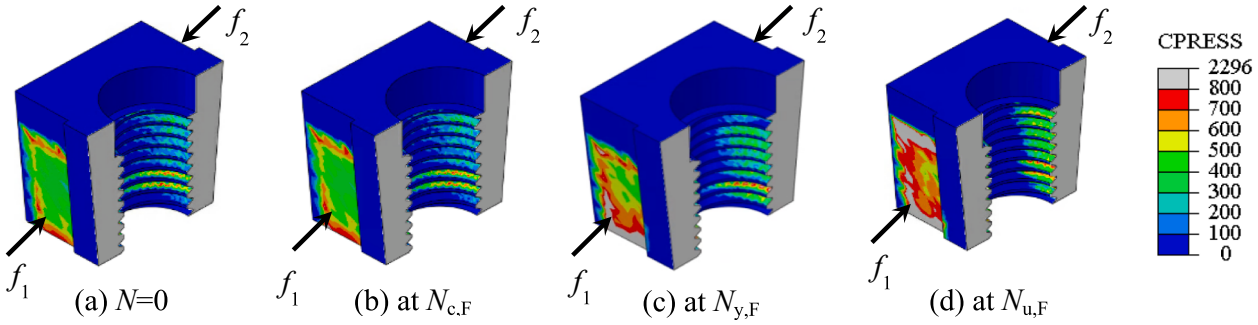

Fig. 21. Development of contact force of the outer wedge.

FE and test results below N_y is neglectable, see Fig. 19 (b). The resulting bolt stress variation is 23 MPa and 14 MPa from FE and test results, respectively. These bolt stress ranges are lower than the constant fatigue limit $\Delta\sigma_D$ of 37 MPa for the M18 bolt with the detail category of 50 [19]. Hence, the bolt behaviour is not critical both for ULS and FLS resistance for WC1.

4.1.3. *Evolution of gap opening*

The opening between two segments has been measured for each specimen during the loading of connection, see Fig. 6. The evolution of the gap opening of WC1 is depicted in Fig. 22, where the gap opening from LVDT Δ_1 is the mean value of the measurements (D2 + D3)/2. Similarly, the gap opening behaviour of wedge connection under uni-axial tensile loading can be separated into three stages with similar boundaries. The gap opening increase to 0.12 mm linearly in the first stage from Fig. 22 (a), followed by an increase until 1.7 mm when the final fracture occurs. It should be noted that the difference between the experimental and FE results at the third stage is apparent, which can be

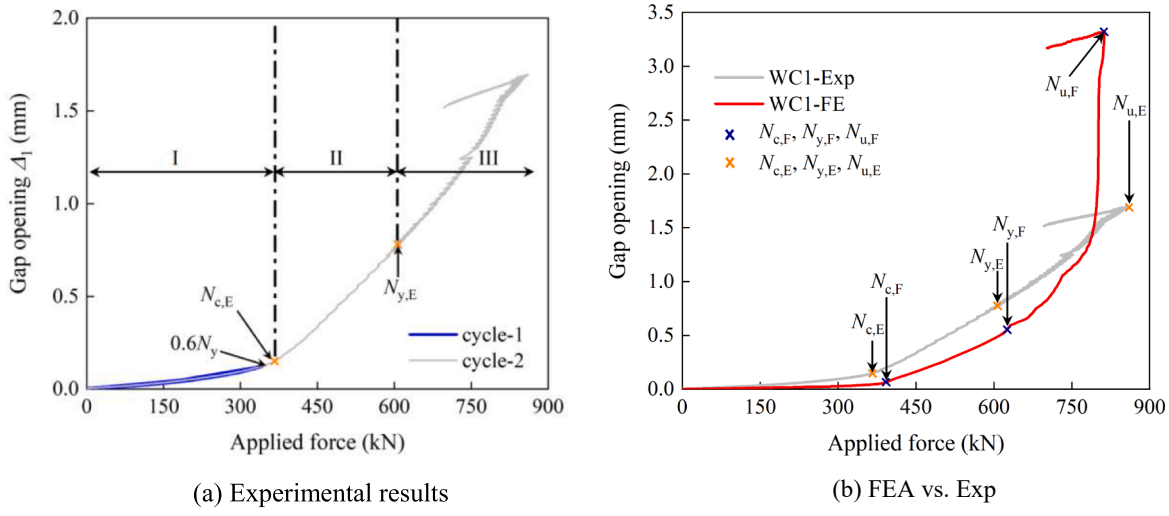

Fig. 22. Comparison of gap opening behaviour between experimental and FE results for WC1.

attributed to the fact that the ultimate deformation capacity of the LVDT was reached.

Fig. 23 compares the gap opening measured from LVDT Δ_1 and between the interface of segments Δ_2 / Δ_3 from FE results. Fig. 5 shows that the force equilibriums of the upper segment and lower segment under external load N_z are:

$$\Delta N_{upper} = N_Z + F_4 - (F_1 + F_2) \quad (10)$$

$$\Delta N_{lower} = F_3 - F_4 \quad (11)$$

According to Fig. 20, ΔN_{upper} and ΔN_{lower} increase at the beginning with a significant decrease in F_4 and a slight increment in F_3. Under the applied force of 100 kN, the resultant force ΔN_{upper} and ΔN_{lower} are 42 kN and 82 kN in tension. The segments have tiny elastic deformation even with low N_z. Therefore, Δ_1 increases at the beginning due to the elastic deformation that occurred in the steel within the range of LVDT. It is observed from Fig. 23 (b) that the existing contact force F_4 is dominantly distributed in the middle of the segment. However, there is no contact force at the edge of the segment. That is why the gap opening Δ_2 opens at $N_z = 280$ kN, while Δ_3 opens until the complete degradation of F_4 at $N_{c,F}$.

4.2. Behaviour of WC2

4.2.1. Failure mode

The load–displacement curves of specimen WC2 are presented in Fig. 24. The curves of FE results agree well with the experimental results. According to Eq. (12), the critical load N_c is different from the one at WC1 with a lower friction coefficient μ of 0.10 and bolt preload P_c of 80 kN. The stiffness degradation ratio ξ is defined as k_i/k_1 to reflect the change of the stiffness during the loading-unloading of the segment specimen, where k_1 is the initial stiffness. The stiffness of the i^{th} cycle k_i is calculated by:

$$k_i = \left(k_{unl,i-1} + k_{rel,i}\right)/2 \quad (i = 2:10) \quad (12)$$

where $k_{unl,i\text{-}1}$ is the tangent stiffness of the unloading path of i-1th cycle, and $k_{rel,i}$ is the tangent stiffness of the reloading path of i^{th} cycle, as shown in Fig. 25 (a).

Fig. 25 (b) shows the stiffness degradation trend with increasing cycles. A drop of 8% of the ξ is observed between the specimen during the 1st and 5th cycle. In terms of the axial load level between the critical load N_c and the yield force N_y, the stiffness reduces gradually at a linear rate from the 2nd to 5th cycle. This can be attributed to the propagation of the local plastic deformation in the segments, as shown in Fig. 26. Beyond the critical load (after the 2nd cycle), the permanent deformation is introduced into the segment successively. The degradation rate increases after the 5th cycle, corresponding to the larger plastic deformation at the lower segment. Despite the cyclic loading, the failure mode of WC2 is similar to WC1 in the middle section at the elongated hole of the lower segment.

4.2.2. Evolution of bolt force

Fig. 27 shows the bolt force change during the cyclic loading. A general trend of bolt force evolution at each loading-unloading cycle is described in Fig. 27 (b). Bolt force increases to some extent during the load path OA, followed by a decreasing trend during the unloading path AB.

The comparison of the bolt force variation $P_{\Delta OA}$ from the test and FE results is shown in Fig. 28 (a), where FE results are basically consistent with the experimental results. In detail, the bolt force keeps constant in the first two cycles. After exceeding the critical load at the 2nd cycle, $P_{\Delta OA}$ increases gradually with the increasing cycles and load levels. $P_{\Delta OA}$ is less than 5 kN when the maximum force of the cyclic loading is below the yield strength of the specimen at the 5th cycle. After that, $P_{\Delta OA}$ increase at a nonlinear and faster rate. The bolt force drops to 0 kN during the unloading path of the 9th cycle. WC2 reached its ultimate strength at the 10th cycle. The results demonstrate that the load capacity of the specimen is not influenced by the loss of the bolt pretension. The maximum bolt stress during the whole cyclic loading is calculated as 420 MPa within the elastic states. Fig. 28 (b) shows the FE model for WC2 is capable of simulating the bolt behaviour accurately until the 8th cycle (under the applied force of 1.25 N_y). This can be attributed to that the applied friction coefficient of 0.1 reasonably mimics the contacts of the pre-lubricated threads. The lubricate states of the practical application of the C1 wedge connection are identical to WC2. Hence, this simulation method is reasonable to reflect the bolt behaviour in the practical application of the C1 wedge connection.

4.2.3. Evolution of gap opening

The evolution of gap opening from LVDT Δ_1 during the cyclic loading from the test is depicted in Fig. 29 (a). The corresponding zoomed-in curves during the loading path of each cycle are shown in Fig. 29 (b).

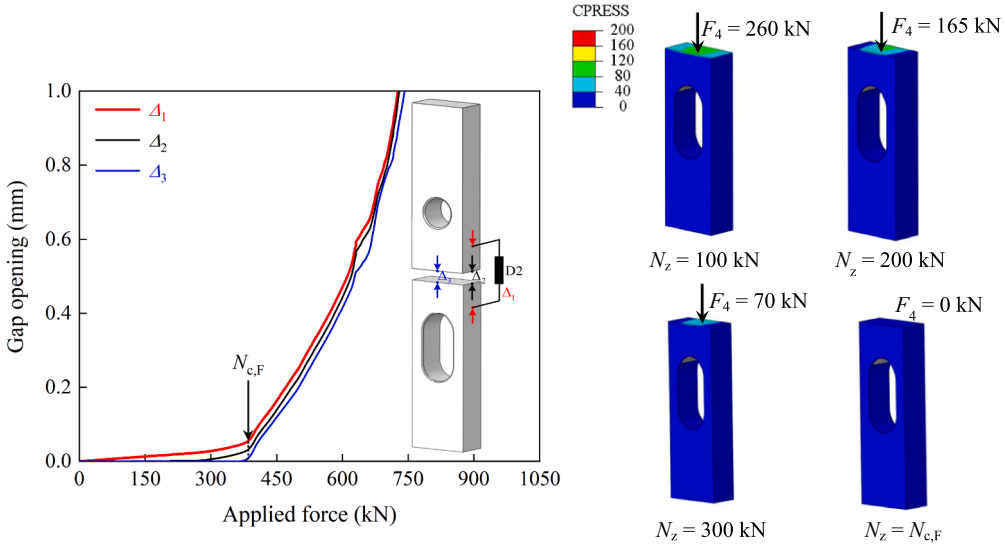

(a) Gap opening behaviour

(b) Contact force in lower segment

Fig. 23. Gap opening behaviour and related contact force.

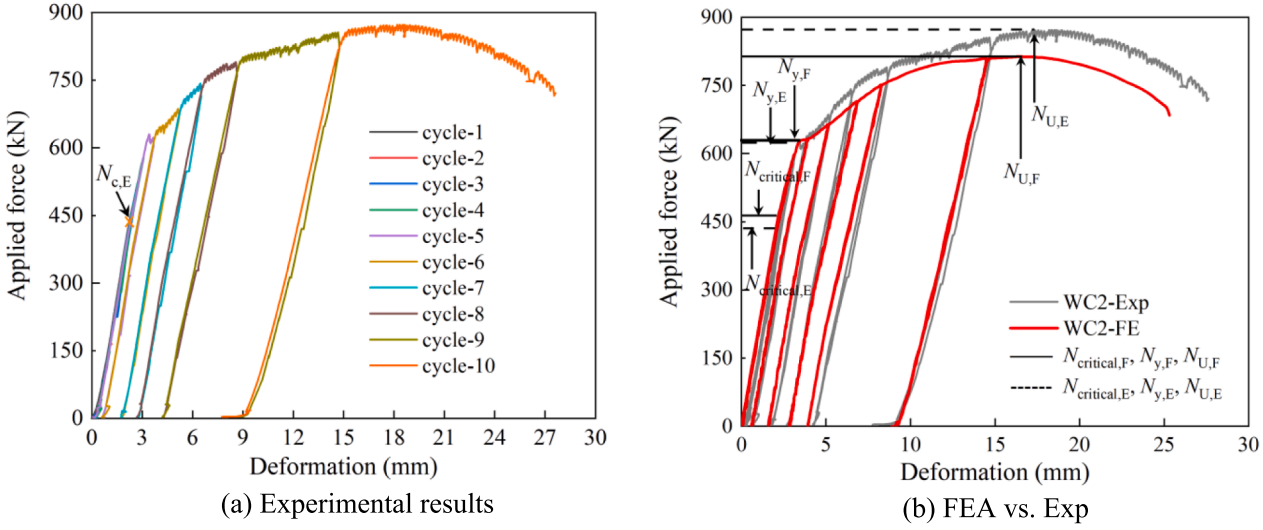

(a) Experimental results (b) FEA vs. Exp

Fig. 24. Load–displacement curves of WC2.

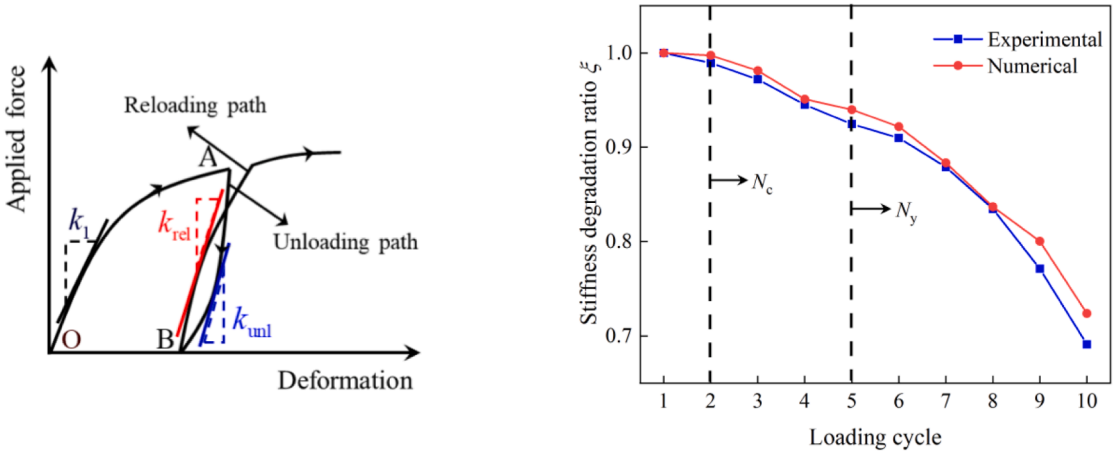

(a) Definitions of stiffness (b) Stiffness degradation curves

Fig. 25. Evolution of stiffness degradation with the number of cycles.

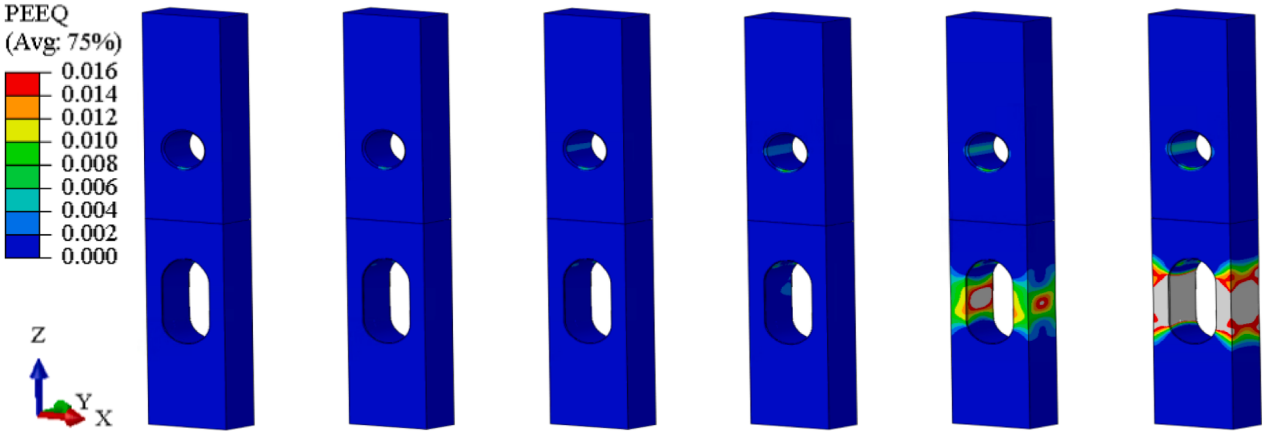

(a) 1st cycle (b) 2nd cycle (c) 3rd cycle (d) 4thcycle (e) 5th cycle (f) 6th cycle

Fig. 26. PEEQ distribution in lower and upper segment at the end of unloading of 1st to 6th cycle.

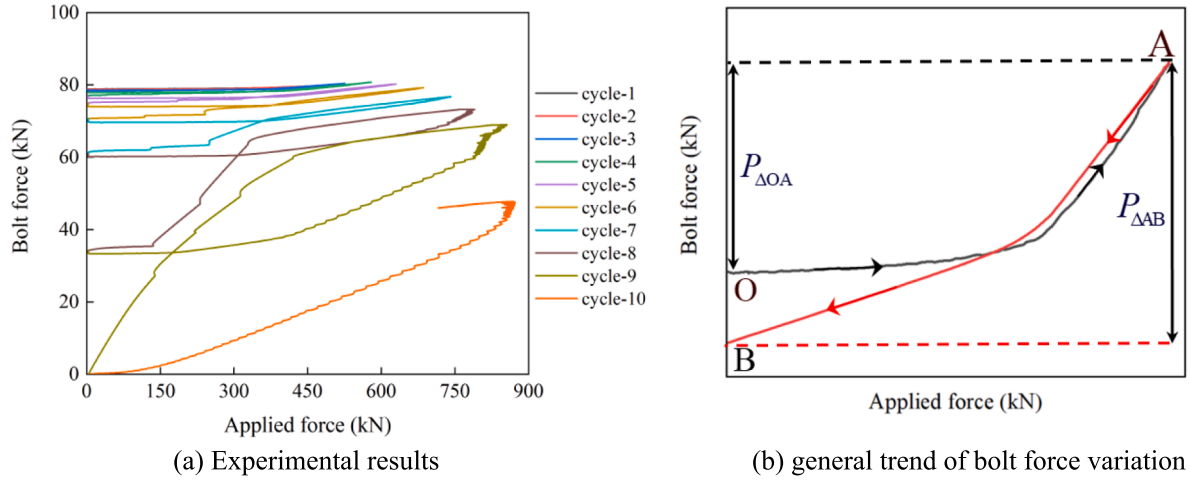

(a) Experimental results (b) general trend of bolt force variation

Fig. 27. Evolution of bolt force of WC2 from the test.

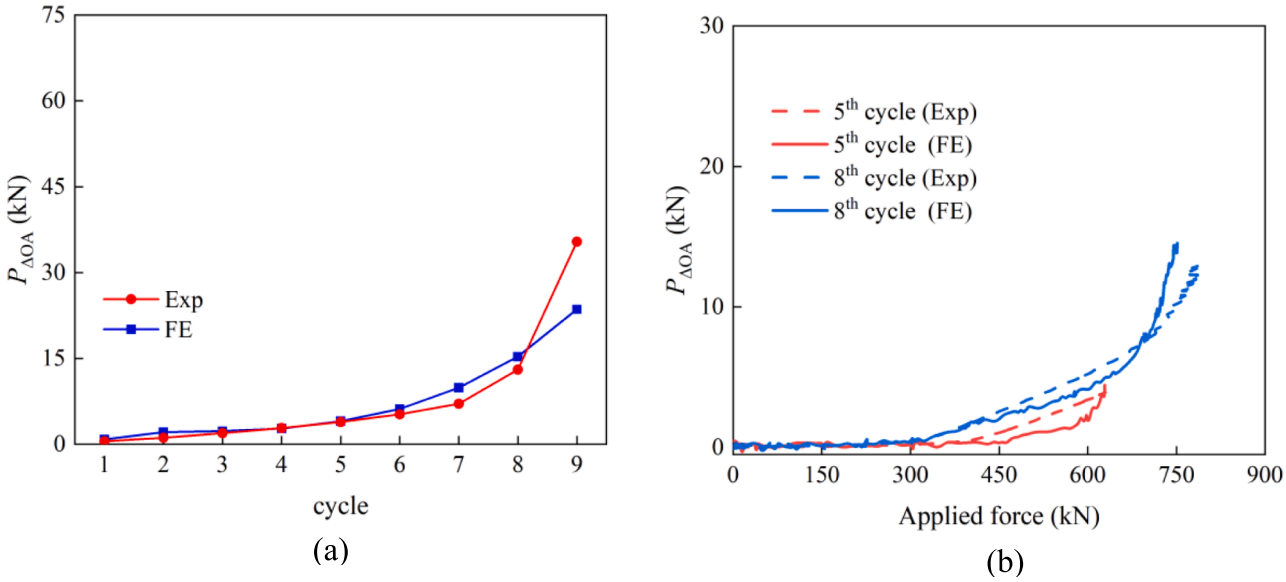

Fig. 28. Bolt force variation during loading-unloading of WC2.

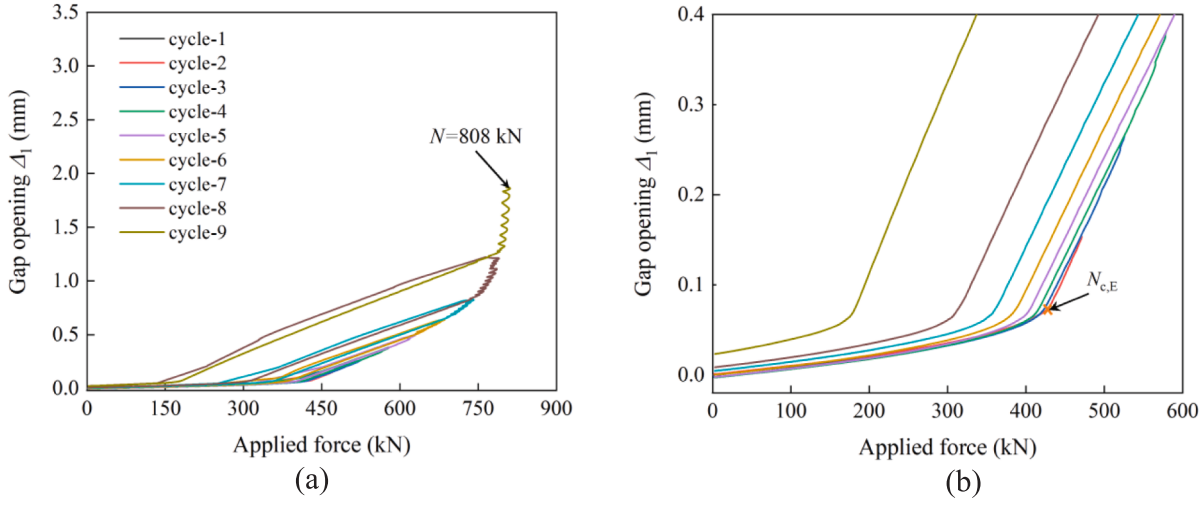

Fig. 29. Evolution of gap opening Δ_1 of WC2 from the test.

The gap opening behaviour after reaching the applied force of 808 kN is eliminated as the ultimate deformation capacity of the LVDT was reached. The envelope of gap opening curves from the test and FE result is compared in Fig. 30 to validate the FE model.

A critical load change ratio ζ is calculated based on the initial critical load after bolt pretension. As shown in Fig. 31, the critical load N_c corresponding to each cycle decreases slightly after the 2nd cycle. A 10% drop is observed at the 5th cycle with the load level N_y. The FE results and experimental results match well, verifying the reliability of the FE model to analyse the cyclic behaviour analysis of the specimen.

5. Parametric analysis

Considering the load cell is not included in practice, the FE model is updated without a load cell to conduct the parametric analysis, as shown in Fig. 32. Table 3 lists the FE models and corresponding parameters. The nominal length of the bolt L_{nom} is reduced from 220 mm to 120 mm in the updated model. The upward displacement is imposed on the reference point RP1 at the top of the segment.

This parametric study aims to quantify the influence of the pre-loading force P_c, the bolt grade, and the friction coefficient between contacts. It should be noted that the influence of the yield strength f_y of the material and the smallest cross-section area A_s of the lower segment on the mechanical performance is not included. This is because their influence is straightforward from the equation $N_u = f_u \cdot A_s$. The displacement at RP1 and gap opening Δ_2 is extracted from the FE results to evaluate the global and local deformation behaviour of the specimens. Based on the discussion in sections 4.1.2 and 4.2.2, it is observed the efficiency of the FE model for simulating bolt behaviour is not influenced by the friction coefficient within the yield strength N_y. The novelty of the C1 wedge connection is the bolt is not the critical component under ULS and FLS. It is necessary to check the bolt stress range $\Delta\sigma_b$ under the applied force range ΔN_z equal to N_y, as listed in Table 3.

5.1. Influence of the bolt grade/friction coefficient

The comparison results between WC-F1 and WC-F2 show that the influence of the steel grade of the bolt is negligible on the global and local deformation capacity. However, the lower friction coefficient μ introduces a higher contact pressure between segments according to Eq. (1). Consequently, the critical load of WC-F3 is higher than WC-F1, see a zoomed-in view in Fig. 33 (a) and (b). The gap opening Δ_2 and bolt force start to increase at 539 kN and 386 kN with the μ of 0.1 and 0.18, respectively. The value of the bolt stress range $\Delta\sigma_b$ of WC-F3 is lower than the one of WC-F1/F2 (see Table 3). The bolt is not involved in the FLS verification for WC-F3.

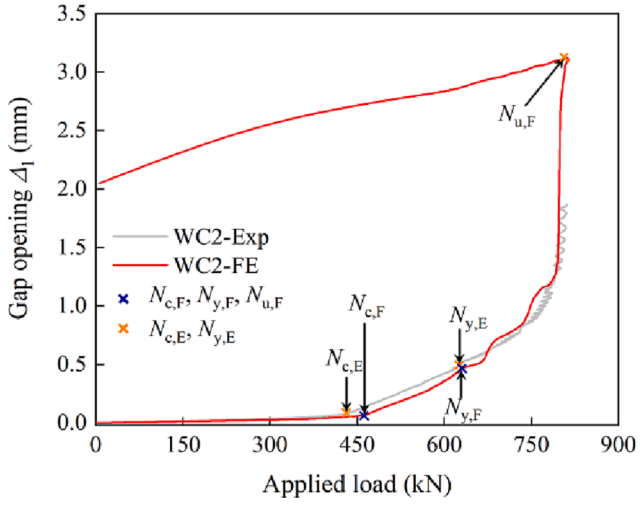

Fig. 30. Comparison of gap opening curves from test and FE results.

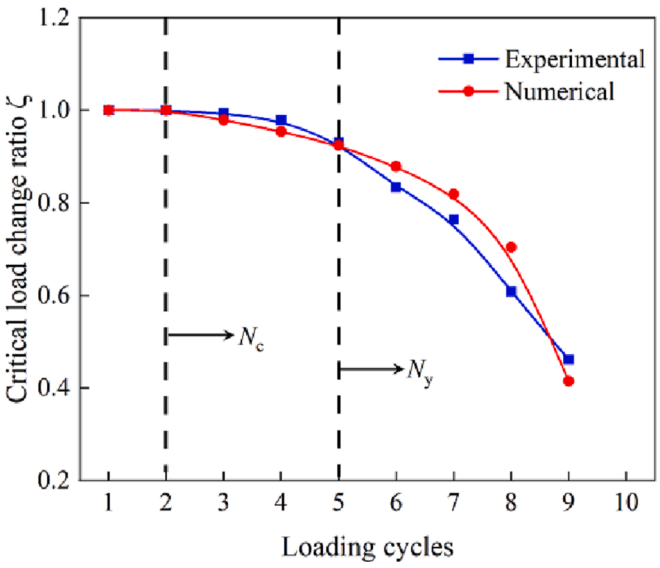

Fig. 31. Change of critical load with the number of cycles.

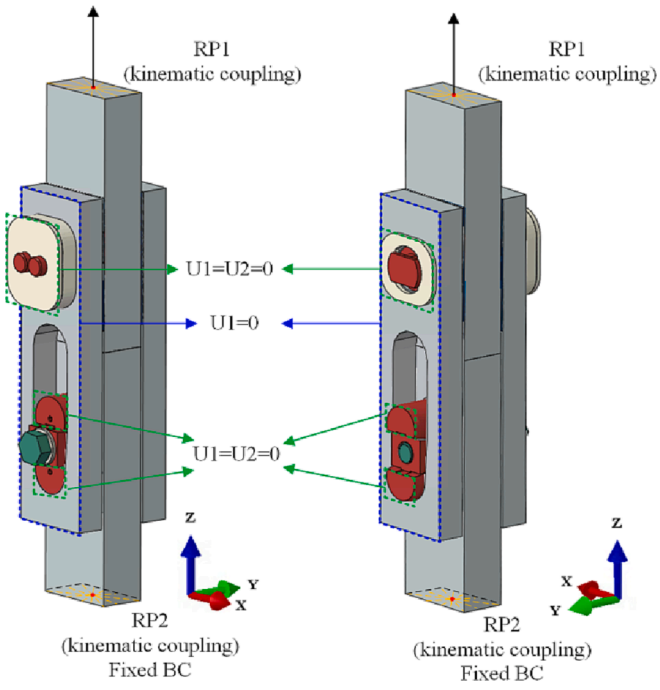

Fig. 32. Updated FE model for parametric analysis.

5.2. Influence of the preloading force

Fig. 34 (a) indicates that P_c has negligible effects on the yield load and ultimate resistance of the specimen. Lower P_c leads to a smaller contact pressure between segments, resulting in a decreasing critical load $N_{c,F}$. The gap opening behaviour of the connection is strongly influenced by the preloading force P_c (Fig. 34 (b)). When P_c is reduced to 50 kN, Δ_2 at the yield load rises to 2.72 times the one with P_c of 95 kN.

As shown in Fig. 35, the bolt stress range needs to be considered for FLS verification when P_c is below 77 kN within the pre-lubricated connection. Accurate application of P_c is necessary in addition to reasonable design of P_c. Table 3 and Fig. 35 reveal that the relationship between P_c and bolt head rotation is linear. The bolt head rotation of 16°

Table 3
Main parameters of the FE model.

Specimen	L_{nom} (mm)	P_c (kN)	Bolt rotation (rad)	Bolt grade	Friction coefficient μ	$N_{c,F}$ (kN)	Bolt stress range $\Delta\sigma_b$ (MPa)
WC-F1	120	95	27.11	8.8	0.18	387	46
WC-F2	120	95	26.11	10.9	0.18	387	46
WC-F3	120	95	34.40	8.8	0.1	546	5
WC-F4	120	80	29.83	8.8	0.1	470	31
WC-F5	120	65	25.76	8.8	0.1	369	67
WC-F6	120	50	21.53	8.8	0.1	285	93

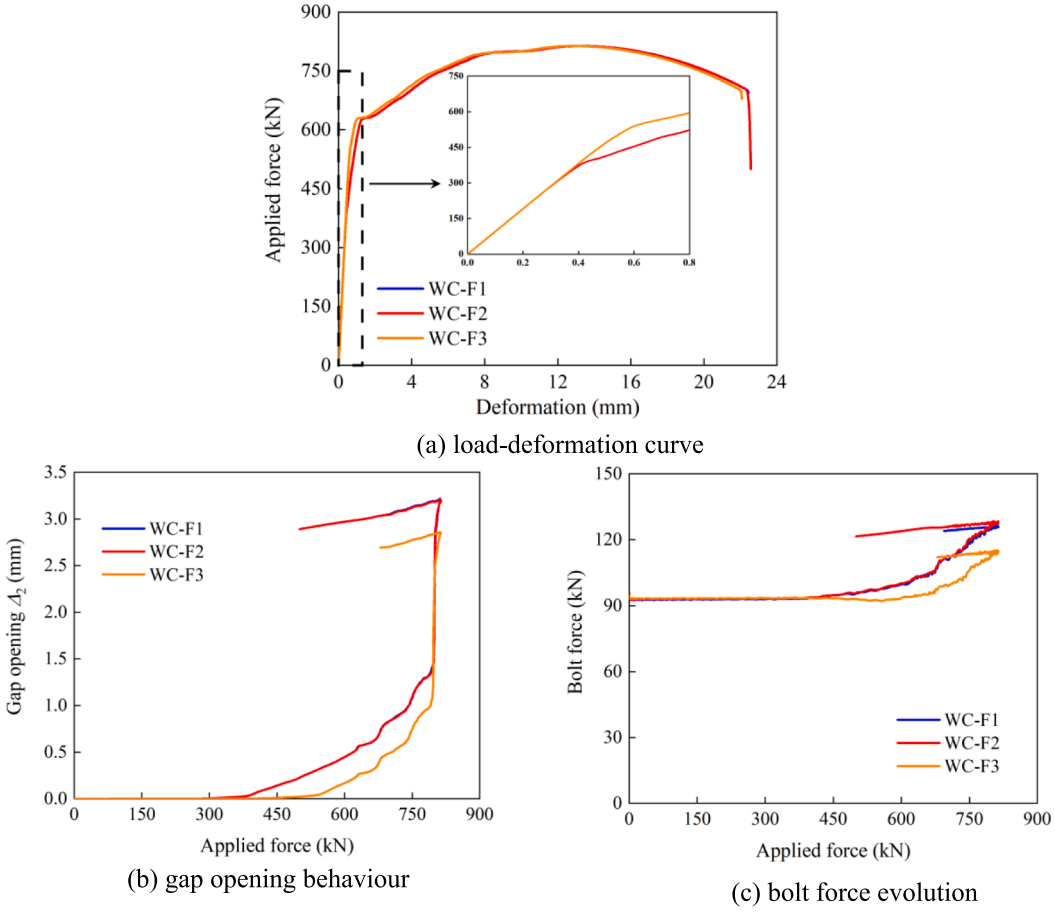

Fig. 33. Results of parametric analysis of bolt grade and friction coefficient.

generates only 1 kN variation in P_c. Therefore the bolt preloading, with assumed friction coefficients, can be easily controlled by the bolt head rotation with high accuracy. Considering $\Delta\sigma_b$ is ignorable within the critical load N_c, the only function of the bolt is to provide the contact pressure at the beginning under the design load lower than N_c.

6. Conclusion

The main characteristics of the 2nd generation of the C1 wedge connection used in large towers for offshore wind turbines are introduced in this paper. An integrated study combining experimental and finite element analysis on its mechanical behaviour is conducted. The following conclusions are drawn:

(1) The bolted ring flange connection loaded in tension transfer force in the upper tower segment by eccentrically positioned bolts. While the C1 wedge connection shows a direct and concentric load transfer. A fairly small lateral bolt preload can be converted to a larger vertical preload in this connection. Under uniaxial and cyclic tensile loading, the failure mode of the C1 wedge connection is net section failure of the lower segment instead of the bolt.
(2) Experimental results under cyclic loading show that stiffness degradation and bolt force variation occurs when the imposed load exceeds the critical load. Moreover, the results demonstrate that the ultimate tensile load resistance of the specimen is not influenced by the loss of the bolt pretension.
(3) The FE analysis matches well with the experimental results. This indicates the proposed FE models could predict the mechanical behaviour satisfactorily and provide evidence for evaluation and further development of the C1 wedge connection both for ULS and FLS design. The FE simulation provides practical guidance to design the connection without bolt failure.
(4) The bolt grade has a negligible influence on the global and local performance of the specimen. On the contrary, the friction coefficient μ and preloading force of the bolt P_c significantly influence the evolution of the gap opening and bolt force. Although the bolt is not critical for the tensile failure mode of the specimen, P_c is also decisive to guarantee the bolt is not involved in the fatigue

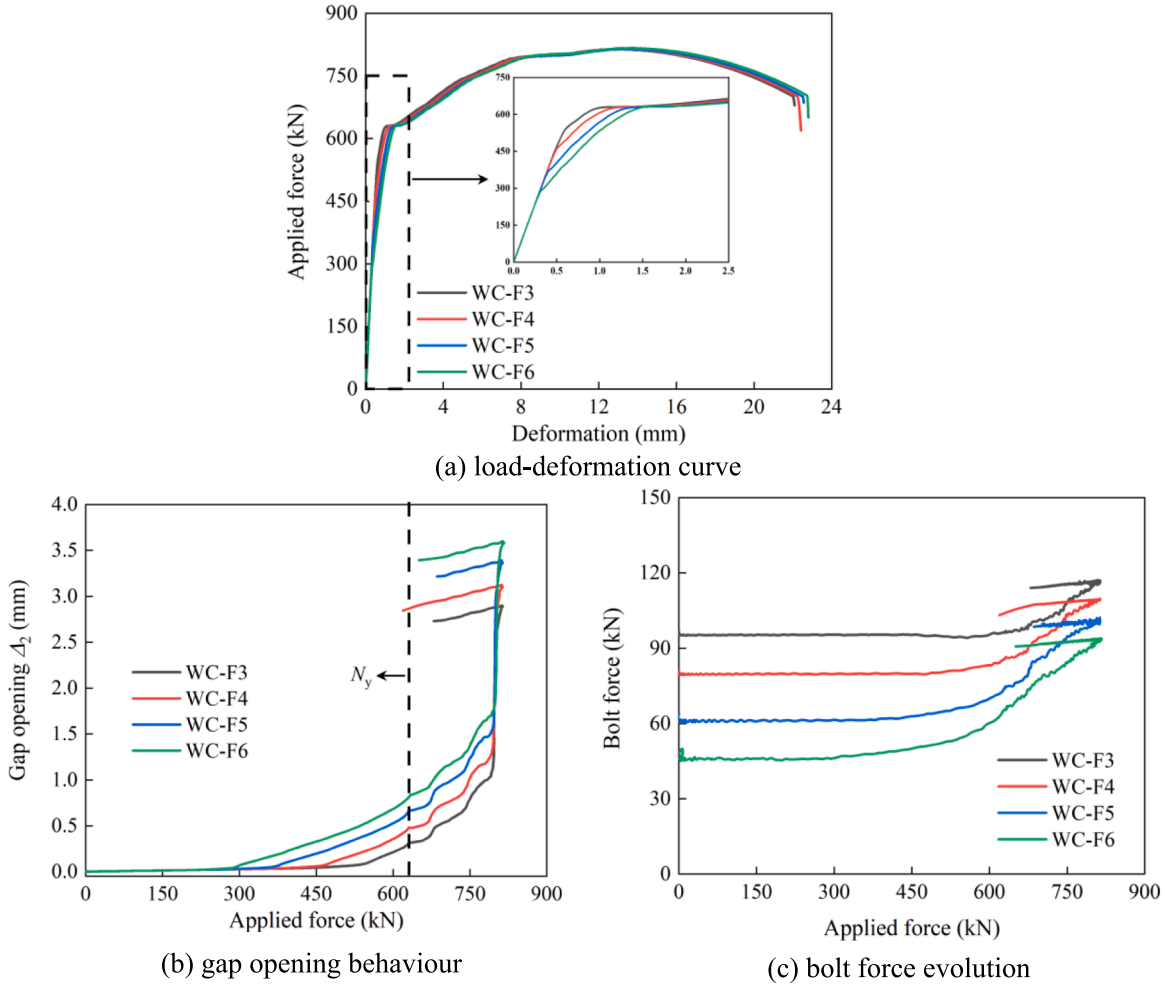

Fig. 34. Results of parametric analysis of P_c.

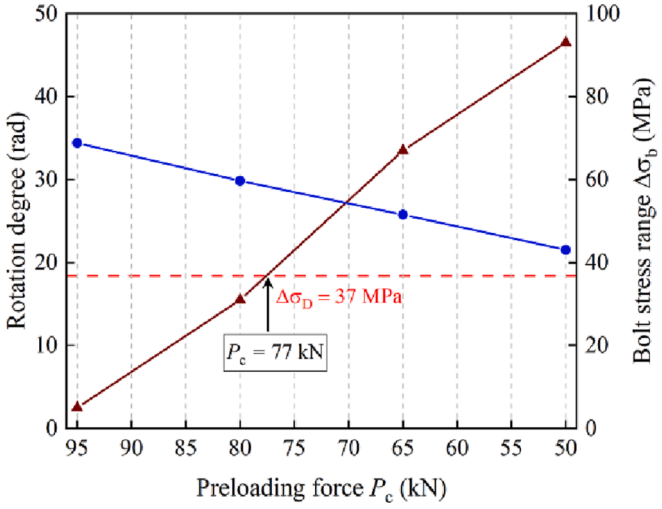

Fig. 35. Response of bolt stress range under different preloading force.

design. It is suggested to design the connection to make sure the design load is lower than the critical load to avoid any bolt damage.

This research focuses on the tensile behaviour of individual segment specimens with C1 wedge connections. It is found that the deformation of the segments is influenced by the free boundary condition of the segment in the experiments. Further investigations are needed to access the effect of the tower continuity on the wedge connection behaviour. To consider the spatial effect and various imperfections, the investigation in full-scale has been performed with dedicated FE analyses by the C1 Connections B.V., which will be published in the future.

CRediT authorship contribution statement

Lu Cheng: Conceptualization, Methodology, Software, Validation, Formal analysis, Investigation, Writing – original draft, Visualization. **Fei Yang:** Conceptualization, Validation, Supervision, Writing – review & editing. **Jasper S tefan Winkes:** Conceptualization, Writing – review & editing. **Milan Veljkovic:** Conceptualization, Supervision, Writing – review & editing.

Declaration of Competing Interest

The authors declare that they have no known competing financial interests or personal relationships that could have appeared to influence the work reported in this paper.

Data availability

Data will be made available on request.

Acknowledgments

The first author wishes to express their gratitude for the financial support of the China Scholarship Council (CSC) under grant number 201806060122. The authors greatly acknowledge Koen Creusen and George Misios from C1 Connections B.V. for sharing experimental data and information about the C1 wedge connection.

References

[1] WindEurope.. Financing and Investment Trends-the European Wind Industry in 2020. Brussels, Belgium. 2021.
[2] Igwemezie V, Mehmanparast A, Kolios A. Current trend in offshore wind energy sector and material requirements for fatigue resistance improvement in large wind turbine support structures – a review. Renew Sust Energ Rev 2019;101:181–96. https://doi.org/10.1016/J.RSER.2018.11.002.
[3] Mehmanparast A, Lotfian S, Vipin SP. A review of challenges and opportunities associated with bolted flange connections in the offshore wind industry. Metals (Basel) 2020;10:732. https://doi.org/10.3390/MET10060732.
[4] Matos R, Shah Mohammadi MR, Rebelo C. A year-long monitoring of preloaded free-maintenance bolts – estimation of preload loss on BobTail bolts. Renew Energy 2018;116:123–35. https://doi.org/10.1016/J.RENENE.2017.05.092.
[5] WindEurope. Offshore wind in Europe - key trends and statistics 2020. https://windeurope.org/intelligence-platform/product/offshore-wind-in-europe-key-trends-and-statistics-2020/; 2021.
[6] Weijtjens W, Stang A, Devriendt C, Schaumann P. Bolted ring flanges in offshore-wind support structures - in-situ validation of load-transfer behaviour. J Constr Steel Res 2021;176:106361. https://doi.org/10.1016/j.jcsr.2020.106361.
[7] Schaumann P, Seidel M, Schaumann P, Seidel M. Failure analysis of bolted steel flanges. In: Proc. Seventh Int. Symp. Struct. Fail. Plast; 2000. https://doi.org/10.1016/B978-008043875-7/50211-2.
[8] Madsen CA, Kragh-Poulsen J-C, Thage KJ, Andreassen MJ. Analytical and numerical investigation of bolted steel ring flange connection for offshore wind monopile foundations. In: IOP Conf. Ser. Mater. Sci. Eng. IOP Publishing; 2017. https://doi.org/10.1088/1757-899X/276/1/012034.
[9] Schaumann P, Eichstädt R. Experimental and analytical fatigue assessment of high-strength bolts for wind turbine structures. 2018.
[10] Schaumann P, Eichstädt R, Stang A. Advanced performance assessment methods for high-strength bolts in ring-flange connections. Stahlbau 2018;87:446–55. https://doi.org/10.1002/stab.201810601.
[11] Amrumbank West. https://www.rwe.com/en/our-portfolio/our-sites/wind-farm-amrumbank; 2022. accessed March 9, 2022.
[12] Humber Gateway offshore wind farm. https://uk-ireland.rwe.com/locations/humber-gateway-offshore-wind-farm; 2022. accessed March 9, 2022.
[13] Nobelwind Offshore Wind Farm, North Sea, Belgium. https://www.power-technology.com/projects/nobelwind-offshore-wind-farm/; 2022. accessed March 9, 2022.
[14] Schaumann P, Frithjof Marten D-I. Fatigue resistance of high strength bolts with large diameters. In: Proc. Int. Symp. Steel Struct. ISSS, Seoul, Korea; 2009. p. 12–4.
[15] Gollub P, Jensen JF, Giese D, Güres S. Flanged foundation connection of the offshore wind farm Amrumbank West – concept, approval, design, tests and installation. Stahlbau 2014;83:522–8. https://doi.org/10.1002/STAB.201410178.
[16] Schaumann P, Eichstädt R, Stang A. Advanced performance assessment methods for high-strength bolts in ring-flange connections. Stahlbau 2018;87:446–55. https://doi.org/10.1002/stab.201810601.
[17] Maljaars J, Euler M. Fatigue S-N curves of bolts and bolted connections for application in civil engineering structures. Int J Fatigue 2021;151:106355. https://doi.org/10.1016/J.IJFATIGUE.2021.106355.
[18] Schaumann P, Eichstädt R. Ermüdung sehr großer HV-Schraubengarnituren [Fatigue of very large HV-bolt assemblies]. Stahlbau 2016;85:604–11. https://doi.org/10.1002/STAB.201610410.
[19] EN 1993-1-9. Eurocode 3: Design of steel structures – Part 1–9: Fatigue. 2005.
[20] BS 7608:2014. Guide to fatigue design and assessment of steel products. BSI; 2014.
[21] Bolt & Beautiful. https://grow-offshorewind.nl/project/bolt-beautiful; 2022.
[22] Veljković M. Emerging technologies for future steel structures. In: Civ. Eng. 2021 Achiev. Visions, Belgrade. Serbia: University of Belgrade - Faculty of civil engineering; 2021. p. 121–31.
[23] The C1 wedge connections. https://c1connections.com/; 2022. accessed March 9, 2022.
[24] Creusen KEY, Misios G, Winkes JS, Veljkovic M. Introducing the C1 wedge connection. Steel Constr 2022;15:13–25. https://doi.org/10.1002/STCO.202100039.
[25] BLUE Wedge Connection, Fatigue Test - TU Delft Scaled 2 - Test Report, RND-01-STGR0202. 2019.
[26] Misios G. Effect on flange waviness on the C1 Wedge Connection. Delft University of Technology; 2019.
[27] C1 connections obtains DNV certification for the C1 wedge connection™. https://c1connections.com/news/c1-connections-obtains-dnv-certification-for-the-c1-wedge-connection/; 2022.
[28] Liu J, Ouyang H, Peng J, Zhang C, Zhou P, Ma L, et al. Experimental and numerical studies of bolted joints subjected to axial excitation. Wear 2016;346–347:66–77. https://doi.org/10.1016/J.WEAR.2015.10.012.
[29] VDI 2230 Part I: Systematic Calculation of Highly Stressed Bolted Joints Joints with One Cylindrical Bolt. 2003.
[30] Cho Y, Lee C, Yee J-J, Kim D-K. Modeling of ductile fracture for SS275 structural steel sheets. Appl Sci 2021;11:5392. https://doi.org/10.3390/APP11125392.
[31] Ling Y. Uniaxial true stress-strain after necking. AMP J Technol 1996;5:37–48.
[32] Yang F, Veljkovic M, Liu Y. Ductile damage model calibration for high-strength structural steels. Constr Build Mater 2020;263:120632. https://doi.org/10.1016/J.CONBUILDMAT.2020.120632.
[33] Yang F, Veljkovic M, Cheng L. Fracture simulation of fully and partially threaded bolts under tension. Ce/Papers 2021;4:156–61. https://doi.org/10.1002/CEPA.1275.
[34] Kanvinde AM, Asce AM, Deierlein GG, Asce F. Void growth model and stress modified critical strain model to predict ductile fracture in structural steels. J Struct Eng 2006;132:1907–18. https://doi.org/10.1061/ASCE0733-94452006132:121907.
[35] Kanvinde AM, Asce AM, Deierlein GG, Asce F. Finite-element simulation of ductile fracture in reduced section pull-plates using micromechanics-based fracture models. J Struct Eng 2007;133:656–64. https://doi.org/10.1061/ASCE0733-94452007133:5656.
[36] Simulia.. Abaqus/CAE User's Manual. Version 6.14. 2016.
[37] Jia LJ, Kuwamura H. Ductile fracture simulation of structural steels under monotonic tension. J Struct Eng (United States) 2014:140. https://doi.org/10.1061/(ASCE)ST.1943-541X.0000944.
[38] Pavlović M, Marković Z, Veljković M, Bucrossed D, Signevac D. Bolted shear connectors vs. headed studs behaviour in push-out tests. J Constr Steel Res 2013. https://doi.org/10.1016/j.jcsr.2013.05.003.
[39] Yahyai M, Kodur V, Rezaeian A. Residual mechanical properties of high-strength steel bolts after exposure to elevated temperature. J Mater Civ Eng 2018;30:04018240. https://doi.org/10.1061/(ASCE)MT.1943-5533.0002416.
[40] Dragoni E. Effect of thread pitch and frictional coefficient on the stress concentration in metric nut-bolt connections. J Offshore Mech Arct Eng 1994;116:21–7. https://doi.org/10.1115/1.2920123.
[41] Tserpes KI, Papanikos P, Kermanidis T. A three-dimensional progressive damage model for bolted joints in composite laminates subjected to tensile loading. Fatigue Fract Eng Mater Struct 2001;24:663–75. https://doi.org/10.1046/J.1460-2695.2001.00424.X.
[42] De Jesus AMP, Da Silva ALL, Correia JAFO. Fatigue of riveted and bolted joints made of puddle iron—a numerical approach. J Constr Steel Res 2014;102:164–77. https://doi.org/10.1016/J.JCSR.2014.06.012.
[43] Braithwaite J, Goenaga IG, Tafazzolimoghaddam B, Mehmanparast A. Sensitivity analysis of friction and creep deformation effects on preload relaxation in offshore wind turbine bolted connections. Appl Ocean Res 2020;101:102225. https://doi.org/10.1016/j.apor.2020.102225.